J. Fluid Mech. (1996), *vol.* 314, *pp.* 53–103

Turbulence, similarity scaling and vortex geometry in the wake of a towed sphere in a stably stratified fluid

By G. R. SPEDDING, F. K. BROWAND AND A. M. FINCHAM

Department of Aerospace Engineering, University of Southern California, Los Angeles, CA 90089-1191, USA

(Received 5 May 1995 and in revised form 24 October 1995)

Late wakes ($Nt > 20$) of towed spheres in a stably stratified fluid were analysed in a plane using a reliable, customized DPIV technique that provides sufficient spatial and temporal resolution to cover all important scales of motion in this freely decaying geophysical flow. Systematic experiments were conducted with independent variation of $Re \in [10^3, 10^4]$ and $F \in [1, 10]$ ($F \equiv 2U/ND$ is an internal Froude number based on the buoyancy frequency, N, and the sphere radius, $D/2$), and for selected $\{Re, F\}$ pairs above this range.

The normalized wake width grows at approximately the same rate as in a three-dimensional unstratified wake, but it becomes narrower, not wider, with decreasing F (i.e. as stratification effects become more important). The centreline defect velocity, on the other hand, reaches values an order of magnitude above those measured for three-dimensional unstratified wakes at equivalent downstream locations. Both observations are argued to be consequences of the very high degree of order and coherence that emerge in the late-wake vortex structures.

Streamwise-averaged turbulence quantities, such as the velocity fluctuation magnitude, and mean-square enstrophy, show similar power law behaviour for all $Re \geqslant 5 \times 10^3$, with exponents equal to those expected in three-dimensional axisymmetric turbulent wakes. There is no obvious physical reason why three-dimensional arguments are so successful in such a flow, and at such long evolution times. The scaling collapses none of the cases for Re below $4 - 5 \times 10^3$, appearing to establish a minimum Re for a class of self-similar stratified wake flows that evolve from fully turbulent initial conditions.

Individual vortex cross-sections appear to be well approximated by Gaussian distributions at all Re, F and Nt studied here. The scaling behaviour of individual vortices mimics that of the statistical, wake-averaged quantities, and differs measurably from a simple two-dimensional viscous diffusion model. The importance of formulating a realistic three-dimensional model is discussed, and some limited steps in this direction point to future useful experiments and modelling efforts.

1. Introduction

1.1. *General background*

The initial formation and subsequent long-time evolution of bluff-body wakes in a stably stratified fluid is of interest both to those concerned with the persistence

of identifiable wake signatures from undersea vehicles, and also as a more general problem, where a localized turbulent mixing event evolves in the presence of contraints due to buoyancy forces. In most cases, the initial Reynolds number can be assumed to be large so that a large range of scales is present and fluid motion is fully three-dimensional over many of them. Although it is well known that at long times, these wakes are characterized by the presence of stable patches of vertical vorticity which have large horizontal length scales compared with any vertical structure, it is not known how these vortices are generated from the turbulent wake in the first place, nor how they evolve at very long times. Neither is the topology of the vortex lines comprising these patches known.

Not only does the stable stratification promote the formation of these high-aspect-ratio vortex structures in the far wake, but it also allows for the transport of energy and momentum by internal waves that can be generated either directly from the body itself (lee waves), or from its wake. At early times, there is the possibility of a coupling of these wave fields with the vortical wake, and certain nonlinear wave–wave interactions are possible. The problem can thus generate a rich set of interesting phenomena, ranging from linear, separable flows composed of regular waves and vortices, to more complex nonlinear interacting flows that are not well understood.

1.2. *Dimensionless parameters*

Far from exterior boundaries, the flow past a body of given geometry is determined by the values of two dimensionless parameters, the Reynolds number, $Re \equiv UD/\nu$ (U is the sphere speed, D its diameter, and ν is the kinematic viscosity), and the internal Froude number, $F \equiv 2U/ND$. F is based on the sphere radius, $D/2$, following the example of Hopfinger *et al.* (1991). F is a measure of the ratio of an advective time scale, $D/2U$, to the time scale, N^{-1}, imposed by the stratification, as measured by the Brunt–Väisälä frequency, $N = \{-(g/\rho_0)(\partial\rho/\partial z)\}^{1/2}$. Thus, at $F \approx 1$, the lee waves reach their maximum amplitude. Within the $\{Re, F\}$ domain generally accessible to laboratory experiment, $F \in [0.1, 10], Re \in [10^2, 10^4]$, widely differing wake dynamics can be observed.

1.3. *Review of recent literature*

Following the early review by Lin & Pao (1979), more recent additions to the literature have clarified some, but by no means all, of these issues in the particular case of sphere wakes in stable stratification.

1.3.1. *Separation lines and near-wake structure*

Sysoeva & Chashechkin (1991), Chomaz *et al.* (1992), Lin, Boyer & Fernando (1992) and Chomaz, Bonneton & Hopfinger (1993*b*, referred to herein as CH93*b*) have documented in some detail the near wake and separation lines on the sphere, with extensive flow visualization in either vertical or horizontal planes. CH93*b* described the appearance of a spiral instability mode in the unstratified wake case for $Re > 4 \times 10^3$. The spiral mode was also present, but with low amplitude for $Re > 800$. The near-wake structure was found to change greatly with the addition of stratification, with only a weak Re-dependence. Nevertheless, for $F > 1.5$, the weak and strong spiral mode regimes were reported to appear at $Re = 4 \times 10^2$ and 4×10^3, respectively. It was suggested that the transition might be related to the move from convective to absolute instability regimes, as described by Monkewitz (1988). Both Lin *et al.* (1992) and CH93*b* report the existence of a regime where separation is almost completely supressed, with a bow-tie-shaped separation line contracting

in both x and y around a critical $F \approx 0.8$. With increasing F, the separation line moves forward in the horizontal plane with respect to the mean flow, and the vertical separation line follows at a higher F so that an elliptical shape is recovered around $F \approx 1.5$, becoming circular with further increase in F. A somewhat similar description was given in Sysoeva & Chashechkin (1991), though $Re \leqslant 800$ was typically quite low.

1.3.2. *Wake spacing*

Both Lin *et al.* (1992) and CH93*b* report an approximately constant power-law decrease in dimensionless shedding frequency, $St = D/\lambda$ or $St = Df/U$, up until $F \approx 3$–4, when St reaches a limiting value of 0.175. This was attributed in CH93*b* to the appearance of the three-dimensional spiral instability, which collapses under the effect of stratification, but sets the initial spacing. The same spiral, or helical mode was observed earlier by Kim & Durbin (1988) in homogenous wakes. The higher Strouhal number regime was associated with Kelvin–Helmholtz instability in the homogeneous case by Kim & Durbin, but CH93*b* interpret it instead as a non-axisymmetric vortex shedding mode at $Re > 800$. Further data points and discussion appear in Bonneton *et al.* (1996), for $1760 < Re < 3890$.

1.3.3. *Late wakes and pancake eddies*

The evolution of the vortex wake structure at moderate and late times has received most attention in Lin & Pao (1979), and recently also in Chomaz *et al.* (1993*a*, referred to herein as CH93*a*). For the moment, late wakes will be defined as those evolving beyond dimensionless times of $Nt \approx 20$. The motion is quasi-two-dimensional in that the vertical component of velocity is very small compared to the horizontal components. In a horizontal plane, the velocity field in that plane is almost completely accounted for by considering the motions induced by vorticity vectors that are aligned parallel to, or close to, the gravity vector. The remaining velocity field corresponds to the 'residual', essentially time-invariant motion described by Lighthill (1996).

In the particular case of turbulent sphere wakes, it is unclear whether partially decorrelated (though not necessarily decoupled), multiple layers form, as occurs in grid-generated turbulence in stably stratified fluids (e.g. Browand, Guyomar & Yoon 1987; Hopfinger 1987). CH93*a* investigated the F-dependence of the far-wake formation, identifying a transitional value, $F = 4.5$ where more than one layer forms in the far wake. It was also observed that rates of vertical diffusion of vorticity in the far wake greatly exceeded a simple viscous diffusion; this could be accounted for by an Ekman pumping type of mechanism, where secondary motion at the vortex patch boundaries increased the diffusion rates to 10–30 times that of simple viscous diffusion. The model would have to be modified somewhat to account for the anticipated multilayer wake at $F \geqslant 4.5$. The decorrelation of vertical vorticity fields at a given Nt was shown to increase with F changing from 3 to 5.

1.4. *Objectives*

This paper reports the results of an experimental programme to study the late wake of towed spheres at comparatively large $\{Re, F\}$, in an attempt to study the effects of independent variations in these parameters, and to identify regimes where the laboratory results can, or cannot, be extrapolated to practical applications, where these numbers tend to be high ($Re \approx 10^6$ and $F \approx 10^2$). The measurement technique allows good spatial and temporal resolution of the instantaneous velocity field on an isopycnal, and the emphasis will be on making specific quantitative estimates

and comparisons of the mean and fluctuating velocity components and their spatial gradients. The focus will be almost exclusively on the vertical vorticity field, as measured at the centreplane behind the sphere. The late wake motions have previously been characterized and described in terms of the patches of vertical vorticity, which will be strongest in the centreplane. It will later become clear that the presence of significant vertical structure, with regions of strong horizontal vorticity, are implied by the centreplane results, but a sufficiently careful investigation of this vertical structure must await further developments in experimental methods. Analysis of the internal wave motions will also be deferred until later. This paper in some ways complements and elaborates upon a previous publication (Spedding, Browand & Fincham 1996) that was based on a small subset of data from the same series of experiments.

2. Quantitative experiments

Spheres of different diameters were towed horizontally through a linear, stable density gradient in a tank with very large horizontal dimensions compared with the sphere radius and initial wake width. A careful application of a customized digitized particle image velocimetry (DPIV) technique allowed the long time evolution of the quasi-two-dimensional flow that results to be measured on an isopycnal. All important scales of motion were fully resolved in space and time, for as long as we cared to continue the analysis.

2.1. *Apparatus*

The tank (figure 1) is a 2.4 m^2 Plexiglas box with a 1.35 m extension to allow for transient and startup effects. Sphere diameters of 1.9, 2.54, 3.8, 5 and 7.62 cm were used, so a minimum of $17D$ was traversed before the sphere emerges into the main tank where all measurements are taken. Since the water depth, $H = 24$ cm, is not always large compared to D, confinement effects must be considered. This is especially important when attempting to isolate Re effects, when the sphere diameter and hence D/H changes. Although boundary effects could be seen in the internal wave field, none of the power law exponents reported here, nor any of the measures of vertical vorticity distribution were affected by changes in D/H over the range of U and D. An example of qualitatively and quantitatively similar wakes for $D/H = 0.08$ and $D/H = 0.32$ will be shown in §3.3.1, figure 12.

Following earlier experiments demonstrating the significant influence on the late-wake flow of a forward-mounted tow wire arrangement, the sphere (figure 2) was mounted with three thin ($d = 0.025$ cm) wires, under (extreme) tension in an inclined plane and suspended between three thicker support cables at the top and bottom of the fluid, respectively. The effects of the top and bottom slider assemblies are confined mostly to the boundaries. Re_d ranges from 7.5 to 65, and shedding can be expected during the high-speed tows, but the wires do not intersect the measurement plane, and no U-dependent perturbation of the measurements at the expected scales was ever detected.

2.2. *Procedure*

The tank was filled with the standard two-tank method to create a linear density gradient with a continuous vertical variation in disolved salt concentration. Once full, the tank was seeded with a high spatial density (in the plane) of neutrally buoyant polystyrene beads, about 0.8 mm in diameter. The beads were sorted by density in a specially constructed columnar tank so that the bead density variation

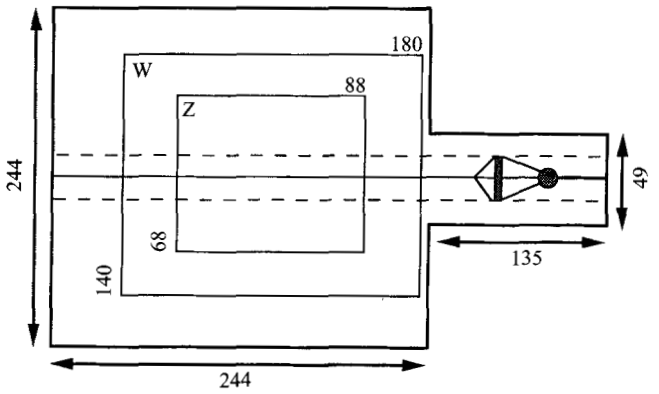

FIGURE 1. Schematic/plan view of tow tank apparatus. All dimensions are in cm. W and Z are areas digitized by CCD cameras with wide-angle and zoom lenses, respectively. The sphere is always towed from right to left, and the startup section serves to avoid contamination of areas W and Z with transient effects.

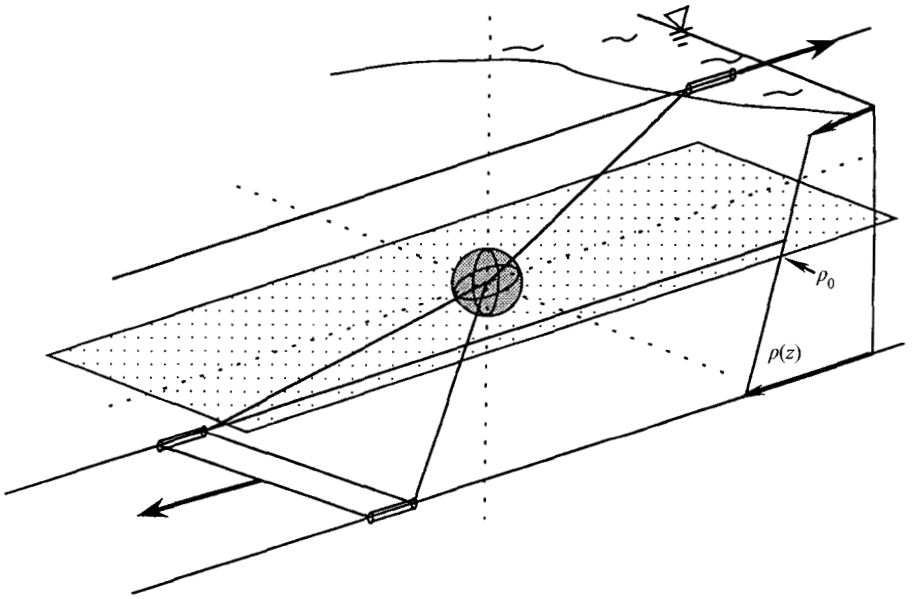

FIGURE 2. Arrangement of tow wires on the sphere. The thick arrows denote tension in main tow cables. The dotted horizontal plane marks the bead sheet, which lies in the centreplane at a particular density, $\rho_0 \pm 0.03\%$, in the linear distribution, $\rho(z)$.

was less than 0.03% ($\rho_0 = 1.0470 \pm 0.00025$). The beads thus mark an isopycnal located at the midplane of the body, to within one bead diameter. The mean density gradient was measured by selective withdrawal from 10 holes in the tank wall, and with a profiling conductivity probe. Restratification of initially turbulent wake motions effectively maintained a constant and linear density gradient for 2–3 days of experiments; i.e. there was very little mixing over the range of $\{Re, F\}$. The relatively inefficiency of mixing under these conditions is consistent with the findings of Park, Whitehead & Gnanadeskian (1994), although their measurements were restricted to $F \leqslant 4.5$, $Re \leqslant 1.6 \times 10^3$. The beads thus remain in a narrow band throughout, and

N varies less than 5% during a series of experiments. F is recalculated to correct for any measurable variations in N.

In each experiment, the bead distribution in $\{x, y\}$ was first homogenized by towing with a vertical rake. After 40 minutes, when the residual kinetic energy and enstrophy densities are more than 3 orders of magnitude below typical initial values in the wake itself, the body was towed the length of the tank, beginning at the far end of the extension section. Data were taken from two parallel-mounted CCD cameras (Panasonic GP-MF552) that differed only in the focal length of the lens, covering areas labelled W and Z in figure 1. For the subsequent DPIV analysis, pairs of video-encoded frames separated by some known δt, were digitized directly into PC RAM. Exposures for both cameras were centred around the same frame time so there is no time shift between the two. At the conclusion of each run, the digitized images were transferred to a networked, cross-mounted disk on a Sun workstation, where all subsequent processing took place.

The entire sequence of events (rake-induced stirring – body tow – data acquisition – data transfer – body return), including timed delays between steps, was automated and could be performed unattended. Consequently experiments could be conducted overnight and at weekends when extraneous disturbances are lower in amplitude and frequency.

2.3. *Data analysis*

2.3.1. *Image pre-processing*

The digitized particle images contain traces from the three large guide cables. The cable images run horizontally across the image, and since they are always at the same location, they were easily removed by replacing affected line segments with uncontaminated neighbours from directly above and below. The line segments were at most 3 pixels in cross-section. This replacement strategy introduces a smoothing and self-correlation pattern that is not important in the DPIV calculation because it is small in size compared with the correlation box size, and it does not introduce any correlation between *successive* images. Tests based on introduction and also subsequent replacement of artificial lines confirmed that the removal could be safely and routinely accomplished in practice.

2.3.2. *DPIV/CIV*

At each time step, two digitized particle images were interrogated and the mean displacement of information in a given subrectangle was computed from the cross correlation peak location. A custom DPIV technique (introduced as Correlation Image Velocimetry (CIV) in Fincham & Spedding 1996) was used to obtain velocities with approximately an order of magnitude improvement in accuracy over standard DPIV methods. The four aspects most responsible are: (i) the decoupling of the interrogation search radius from the correlation box size; (ii) the use of a variance-normalized correlation; (iii) an iterated smoothing-spline interpolation/fitting method for accurate fitting of the correlation peak, and (iv) a direct computation of the cross-correlation, without the use of FFTs. Arbitrary sizes and shapes of correlation boxes can therefore be finely tuned to the properties of the local displacement field. The method does not depend on the presence of particles, but is a localized image texture correlation; particles are just convenient fluid markers which ensure that the image texture motions map closely onto fluid motions.

2.3.3. *Error estimates*

The uncertainty in estimating the velocity vector of a local, correlation-box-sized blob of fluid is not a simple function of velocity magnitude, and so cannot honestly be expressed as a fixed percentage. The error in determining a cross-correlation peak location is, to a rough approximation, fixed in pixels, at ≈ 0.02 px, regardless of the displacement. The true error depends also on the magnitude of the local in- and out-of-plane velocity gradients across measurement volume, whose size is determined by the correlation box size and the light or bead sheet thickness. Extensive simulations and experimental verifications indicate that practical measurement errors of 0.05 px are attainable. When mean displacements are of the order of 5 px, the mean expected uncertainty in velocity is thus 1%.

Given that the real error depends on the flow field *structure*, it is very important to optimize the effective exposure time, δt, so that the velocity bandwidth is maximized. The bandwidth is bounded by the limits in spatial resolution at the lower end, and by the largest length scale that must be resolved at the upper limit. In the decaying wake flow, δt should increase exponentially with time at a rate that matches the decay in energy and enstrophy of the wake flow. The decay rates were estimated in initial experiments, and were then used to generate the timing exponents for the experiments reported here. The decay rates measured in this paper are being used for the same purpose in current experiments.

2.3.4. *Estimation of velocity gradients*

The velocity vectors were reinterpolated onto the regular interrogation grid to correct for systematic errors from the finite displacement of the particles during the effective exposure time, δt. The interpolation was calculated from a least-squares estimation of coefficients for a two-dimensional, smoothing spline (Spedding & Rignot 1993), that also therefore gives analytic formulae for reconstruction of the spatial velocity gradients. The usual errors stemming from finite differencing techniques were thus avoided, and the error in quantities derived from the spatial gradients is at most 10% of the local mean value.

2.3.5. *Spectral filtering*

Provision must be made for removal of noise. Here the principal sources were from instability and uncertainty in the CCD camera synchronization signals, and from systematic errors in correlation peak location due to the bias introduced by non-uniformity in the information location in the discretized signal. Since we wish to retain the fidelity of velocity gradient information, a simple global smoothing is not acceptable, and a two-pass filter system was devised. A first pass involves the smoothing spline interpolation discussed above, followed by filtering with a fourth-order Butterworth low-pass filter with cutoff wavelength set at 1.5 times the grid spacing. Selective removal of small-scale noise at scales of the size of the grid mesh is justified on the grounds that such fluctuations are just as likely to be artifacts as data, and the original 50% overlap on the interrogation boxes adds further support. A simple spectral filter will itself contaminate the data, by implicitly imposing periodic boundary conditions on data that are not periodic. The quasi-periodic error was reduced by performing mirror-image reflections about each edge, and at the corners, performing the FFT on the $3m \times 3n$ grid, and retaining only the central $m \times n$ domain upon inverse. The smoothed, gridded velocity field was then used as input to a second pass where spatial gradients were computed from patched, local spline functions. The splines have a smoothing parameter, ρ_s,

that can be controlled according to local flow properties. Smoothing was applied only within an envelope of possible values that caused fluctuations in the mean r.m.s. velocity of less than 1%. No smoothing was permitted when changes of greater than 5% in peak $\{u,v\}$ resulted, or when peak values of ω_z (of either sign) changed by more than 5%. The detailed procedure is one that allows evident noise contamination to be trapped, but is conservative so as to maintain confidence in the derived quantities of vorticity and divergence (in the plane) that are discussed in the next section.

The sensitivity to velocity gradients is achieved at the expense of tolerating certain systematic artifacts, that are most noticeable in low-*Re*, low-*F* flows where a strongly localized wake flow is surrounded by fluid that is essentially at rest. Where the true velocity gradients are very weak (essentially zero across the interrogation box), an artificial $\partial u/\partial y$ is measured due to the resonance of a peak-locking in the cross-correlation peak-fit algorithm with the finite precision of the video digitizer in phase-locking onto each successive line of the incoming video signal. The precision is limited by the clock period, which is 1/20 MHz = 50 ns. Average uncertainties of the order of 25 ns are thus unavoidable. We claim to measure pixel displacements of 0.05 px, which, for a 512 × 480 image at 30 Hz framing rate, is equivalent to a time resolution of approximately 7 ns. Consequently, in the absence of any other correlation information, it is *expected* that the phase errors in video digitizing will be measured. That is exactly what is observed in the outer flow fields of figures 4, 7 and 8. Excepting one comparison of inner and outer wake energy and enstrophy densities (figure 16), the outer part of the flow field (by definition) takes no part in the quantitative analysis that follows. In the inner wake region, for which the experimental parameters were tuned, the amplitude of this error is lost in the mean correlation peak displacements that are (correctly) caused by motion of the tracer particles in the fluid.

2.3.6. *Effective resolution / discretization errors*

Although some care has been taken to avoid excessive smoothing of the velocity field, the CIV method, like all discrete imaging methods, will always smooth out and underestimate scales that are below, or close to the grid scale. The smallest scale at which undersampling becomes unavoidable is determined by the interrogation box size (in pixels), which in turn depends on the particle seeding density. Further smoothing occurs due to 50% overlap of interrogation boxes, and from the explicit procedures described above. The physical scale to which the true sampling corresponds depends partly on the geometry of the optics. By using two cameras simultaneously, with different focal length lenses, two independent measurements can be cross-checked, and the fine-scale grid can be used to check the possible undersampling effects on the coarse grid. For convenience, the grid size in both cases was 70 × 56, giving average grid spacings of 2.54 cm and 1.24 cm, respectively. For $Re > 10^3$, and sphere diameters between 1.9 and 7.62 cm, one can expect scales smaller than the Nyquist criterion to be present at initial times, and at some later time, the fine mesh will correctly resolve scales that are still below the resolution of the coarse mesh. The effect can be observed in departures from power law behaviour of certain of the wake-averaged quantities described below. When it occurs only in the coarse mesh, those data can be discarded. When and if a similar roll-off (at small Nt, or x/D) appears in the fine mesh data, it is reasonable to assume a similar cause, and these data can also be omitted.

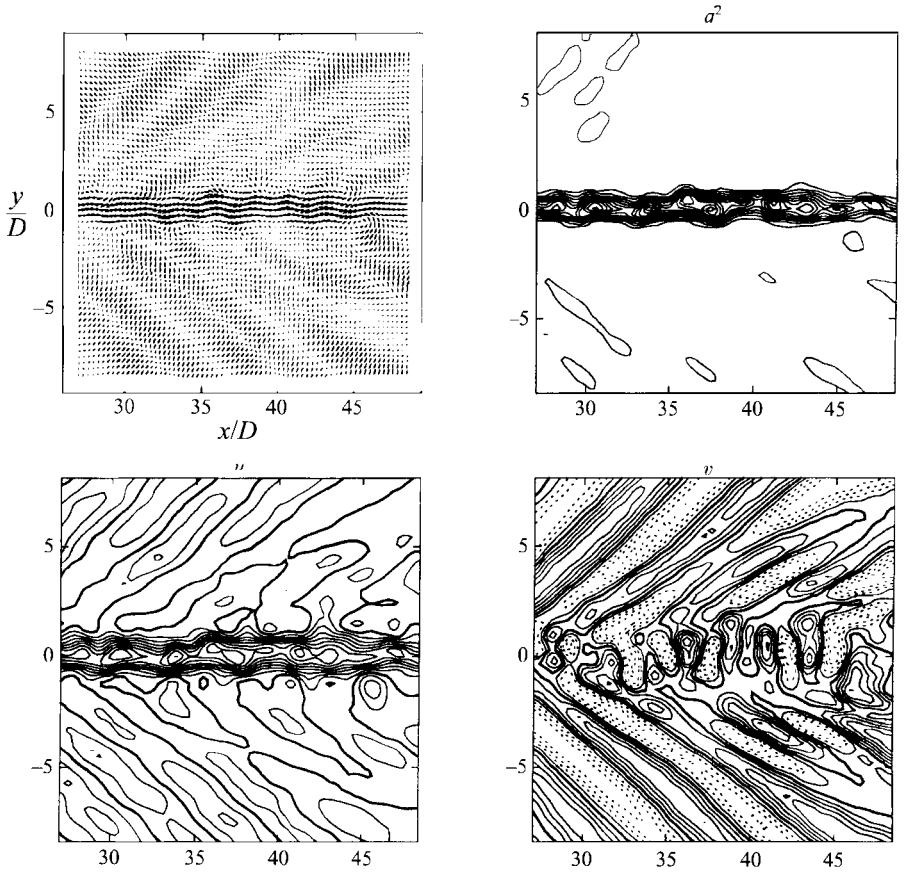

FIGURE 3. Example velocity field for $F = 1.2, Re = 4877, Nt = 44$, shown as velocity vectors, $\{u,v\}$, and contours of constant q^2, u and v. In the u and v contour plots, the zero line is thickened. There are 13 equally spaced contours in q^2, u and v, with intervals of $\Delta q^2 = 0.142$, $\Delta u = 0.142$ and $\Delta v = 0.074$, respectively.

2.3.7. *Separation of internal waves and vertical vorticity*

Let $\{u,v,w\}$ be the components of velocity in $\{x,y,z\}$, where g acts in the $-z$ direction. $\{u,v\}$ are the horizontal components of velocity that can be estimated. In all experiments described here, u and v are measured at $z = 0$, on the centreplane behind the sphere. Figure 3 shows an example of a measured velocity field, at a comparatively early time, $Nt = 44$. The vectors give an idea of the spatial resolution. A strong internal wave field can be seen together with recirculating motions in both the $\{u,v\}$ and their separate component fields. The velocity vectors are actually projections onto the $\{x,y\}$-plane of $\{u,v,w\}$ at discrete points on an isopycnal. This is a reasonable approximation of $\{u,v\}$ in a plane of constant z, when vertical displacements are small. Let $\boldsymbol{q}$ be this estimate of $\{u,v\}$. At any z, one can separate $\boldsymbol{q}$ into

$$\omega_z = \nabla \times \boldsymbol{q}, \tag{2.1}$$

and

$$\Lambda_z = \nabla \cdot \boldsymbol{q} \tag{2.2}$$

Equations (2.1) and (2.2) represent an experimental analogue (specific to the single, horizontal plane of measurement) of the decomposition of Riley, Metcalfe & Weissman (1981) and Lilly (1983), who showed that in the low-F limit, one can separate wave motions with time scales $O(N^{-1})$ and amplitudes in z of $O(1)$, from turbulent motions with time scales $O(N^{-1}/F)$ and $O(F^2)$ vertical motion. Here, F cannot always be regarded as small (at least at early times), and $\Delta_z = -\partial w/\partial z$ (from continuity) will contain contributions from both waves and turbulence. The 'waves and turbulence' description of equations (2.1) and (2.2) is thus a convenient approximation, and not a strict separation. As the measurement occurs on a constant-density surface, the vortex- and wave-dominated parts might be more properly associated with the wave/potential vortex decomposition introduced by Staquet & Riley (1989). A general discussion of the comparative merits of alternative velocity field decompositions in Fourier space with application to DNS in stably stratified turbulence can be found in Lesieur (1993).

Figure 4 shows the representation of the experimental $\boldsymbol{q}(\boldsymbol{x})$ field of figure 3 as ω_z and Δ_z. The figure also shows the colour coding for all subsequent flow field images, where the colour bar is always rescaled at each local timestep, and balanced about the zero level at mid-point along the colour bar.

Given Δ_z, the amplitude of the internal waves can be calculated, based on relations given by linear wave theory (e.g. Lighthill 1978, 1995). A separate paper will focus on the internal wave structure, comparing experimentally derived Δ_z estimates with theoretical predictions. Remarks here will be restricted mostly to qualitative statements, but it should be noted that the assumption of two orthogonal, and separable vorticity components is an approximation only, justifiable mostly at late times when the local Froude number is low. At early times, both the sphere and its initially turbulent wake can generate and organize structures where the vorticity vector can have any intermediate direction.

2.3.8. *Wake energy, enstrophy and dissipation*

Since both the velocity field and its spatial derivatives are known with good accuracy, it is possible to remark on the vortex dynamics of the flow and also to measure certain spatially averaged quantities. In particular, X-averaged measurements can be made to generate mean flow profiles. Taking X-averaged statistics at fixed times is equivalent to averaging over a certain downstream portion of the wake in body coordinates. Ideally, the averaging domain, ΔX, should be a small fraction of the total wake length, X. At long times, and for large F, this is so. The general expression for $\Delta X/X$ is

$$\frac{\Delta X}{X} = \frac{\Delta X/D}{Nt\,F/2}.$$

A wake width, L_W, can be defined by computing a ΔX-averaged velocity profile, $U_X(y)$, where $\Delta X = 1.8$ m, or 0.88 m, is the streamwise length of the measuring area (figure 5), and L_W can be taken as the distance in y where $U_X(y) > 0.2U_0$, and U_0 is the mean centreline velocity. Alternatively, twice the standard deviation of the ΔX-averaged $\omega_z(y)$ profile can be used, although this was found to be a little less smoothly varying in time. At each timestep, L_W was used to define inner wake and outer ambient flow domains. Spatially averaged quantities within the wake region will be denoted by $\langle\rangle$-brackets, so, defining $q = (u^2 + v^2)^{1/2}$ the local (inner wake) energy density is

$$E = \tfrac{1}{2}\langle q^2 \rangle. \tag{2.3}$$

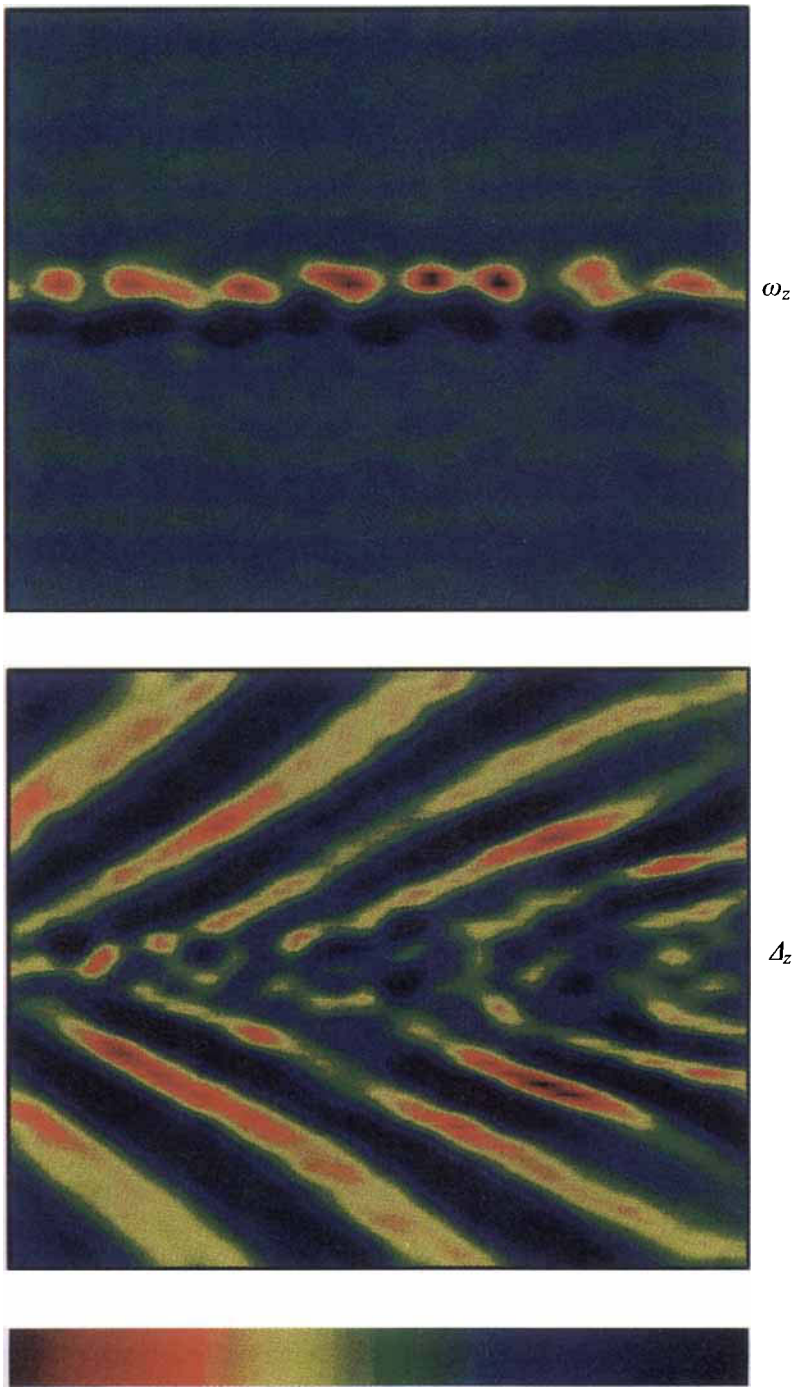

FIGURE 4. Separation of $\boldsymbol{q}$ in figure 3 into its vortical- and internal-wave-dominated components, ω_z and Δ_z.

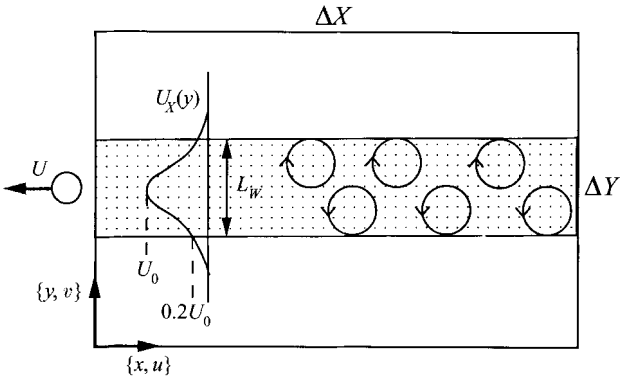

FIGURE 5. Wake geometry definitions. Streamwise-averaged velocity profiles taken over the length ΔX are used to define the wake width, L_W. The data domain, $[\Delta X, \Delta Y]$, is 180×140 cm, or 88×68 cm for areas W and Z of figure 1.

Similarly, given the vertical vorticity

$$\omega_z = \frac{\partial v}{\partial x} - \frac{\partial u}{\partial y}, \tag{2.4}$$

then the local mean enstrophy is

$$W = \tfrac{1}{2}\langle \omega_z{}^2 \rangle. \tag{2.5}$$

The measurable components of the rate of strain tensor are

$$s_{ij} = \frac{1}{2}\left(\frac{\partial u_i}{\partial x_j} + \frac{\partial u_j}{\partial x_i}\right), \quad i,j = 1,2, \tag{2.6}$$

and, denoting ϵ_z as the kinetic energy dissipation rate due to velocity gradients in the plane normal to z, then the mean value, S, in the inner wake region is

$$S = \langle \epsilon_z \rangle = 2\nu \langle s_{ij} s_{ij} \rangle. \tag{2.7}$$

3. Results

3.1. $\{Re, F\}$ *domain, naming conventions*

The experimental conditions were chosen such that independent variations of both F and Re can be followed as shown by the rectangular grid in figure 6. Each data point represents at least one fully resolved, logarithmically spaced time sequence of 64 steps, for each camera. Together with 6 further outlying points with larger F and/or Re, figure 6 represents a database of $29 \times 128 \simeq 3700$ instantaneous velocity fields.

We shall adopt a naming convention where each horizontal track at constant Froude number, F, will be called Fn, where n is the nearest integer of the mean F, and each vertical track will similarly be named Rn, where n $= Re \times 10^3$. R10 thus denotes the series of increasing F, for $Re \simeq 10^4$. Each series is fixed in one parameter, and is always in increasing order with respect to the other. When individual points in a series are referred to, they are named with an extension of this same integer representation of the second, varying parameter. So, for example, the point F4.5 is for $F = 4, Re = 5 \times 10^3$, and it is the same as R5.4.

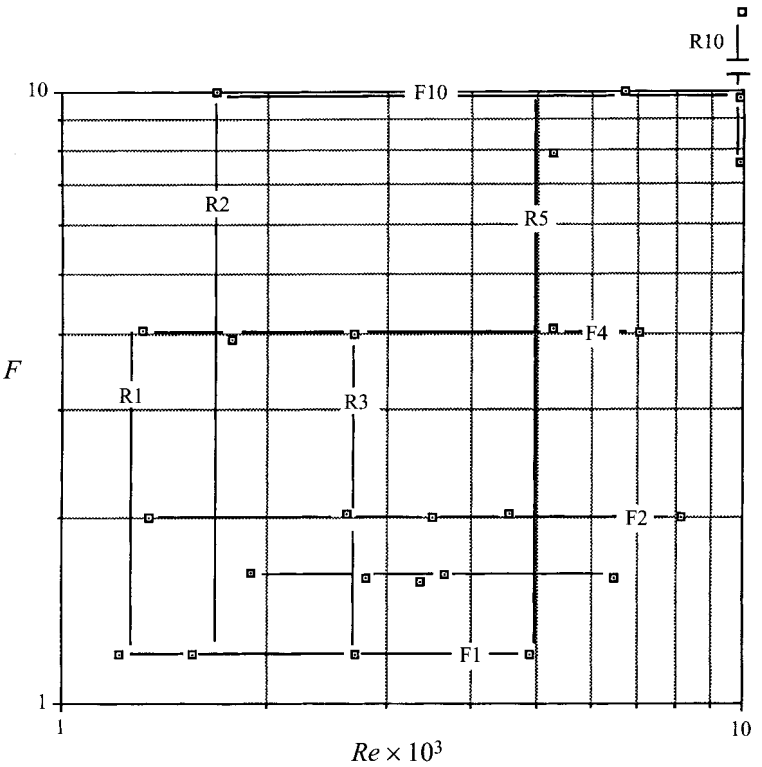

FIGURE 6. $\{Re, F\}$ domain for stratified wake experiments. Solid lines mark tracks of approximately constant Re or F. Figures 7(*a,b*) and 8(*a,b*) are taken from tracks R5 and F10, respectively.

Although the following discussion will be informed by the analysis of all points on figure 6, it is impracticable to attempt to show all the supporting ω_z and Δ_z fields. Most of the remainder can be viewed online over the internet using a point-and-click forms table that roughly corresponds to figure 6 in layout. Instructions as to how to use the World Wide Web protocol to do this are in the Appendix.

3.2. *Qualitative remarks on the variation of* $\omega_z(x, y, Nt)$ *with* $\{Re, F\}$

In this section, certain general trends with Re and F can be noted with particular reference to two tracks, R5 and F10, in the $\{Re, F\}$ domain of figure 6. The parameters describing the experimental conditions are in table 1. We note that figures 3 and 4 indicate that the internal wave motions are closely associated with the initial undulation of the mean wake profile, and the initial formation of coherent patches of ω_z. This interesting interaction is most noticeable at low $\{Nt, F\}$ and will be discussed in a future publication, and ignored here. Quantitative wake spacing measurements in §3.4 show that the omission is mostly justified, as less exotic mechanisms can be invoked to account for most of the data.

Figure 7(*a*) shows $\omega_z(x, y, Nt)$ for four different values of F, at $Re \simeq 5 \times 10^3$. At each F, the time series from left to right shows a number of vortex merging events up to $Nt = 245$. The wake structure otherwise remains quite regular, and vortices remain close to the centreline. At later times still (figure 7*b*), few neighbour interactions can be seen; the column at $Nt = 500$ is essentially repeated at $Nt = 820$. The vortices grow in size, apparently diffusively ($Nt = 1270$), and can be distinguished above the background even up to $Nt \simeq 2000$ in the far right column. A principal result, that

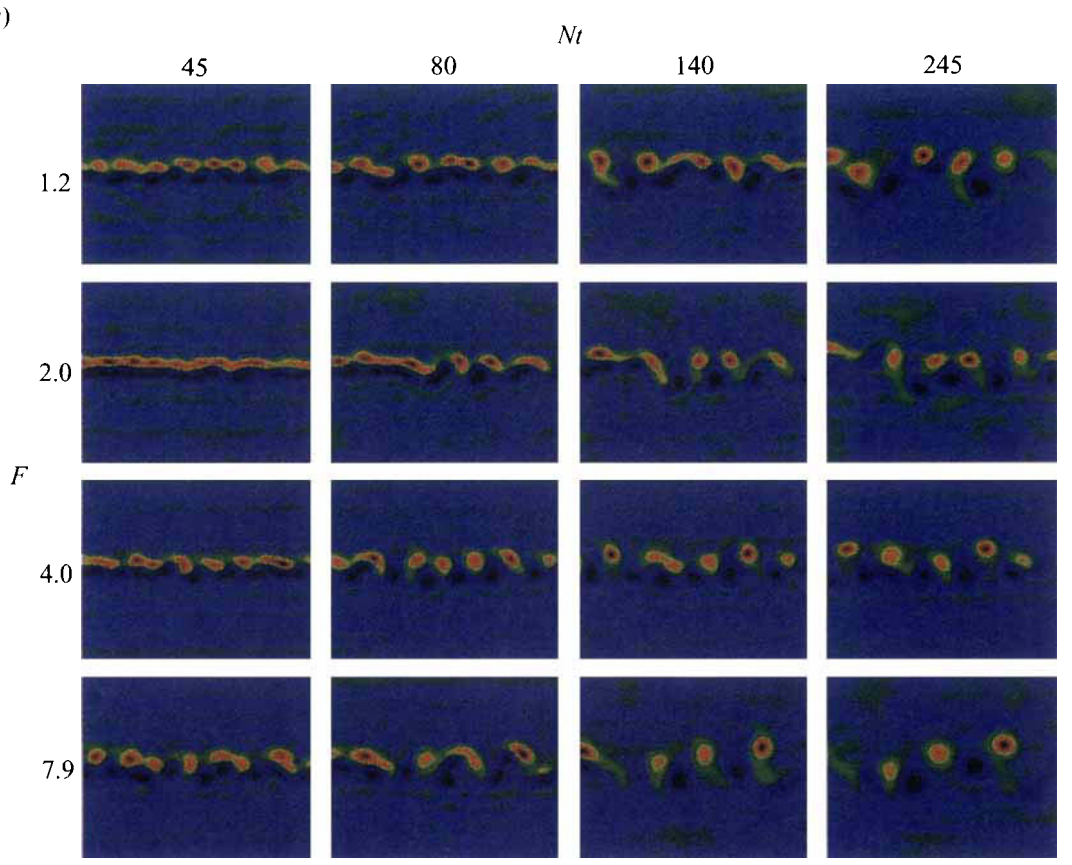

FIGURE 7 (*a*). For caption see facing page.

Exp.	N (rad s^{-1})	D (cm)	U (cm s^{-1})	Re	F
R5.1	1.4	7.6	6.4	4880	1.2
R5.2	1.8	5.0	9.1	4550	2.0
R5.4	1.8	3.8	13.9	5285	4.0
R5.8	0.9	3.8	13.9	5285	7.9
F10.2	0.9	1.9	8.9	1685	10.0
F10.3	1.8	1.9	17.4	3300	10.2
F10.7	0.9	3.8	17.7	6715	10.0
F10.10	1.4	3.8	26.0	9880	9.8

TABLE 1. Experimental details for R5 and F10 series. Values are rounded to one decimal place. *Re* is rounded to the nearest 5.

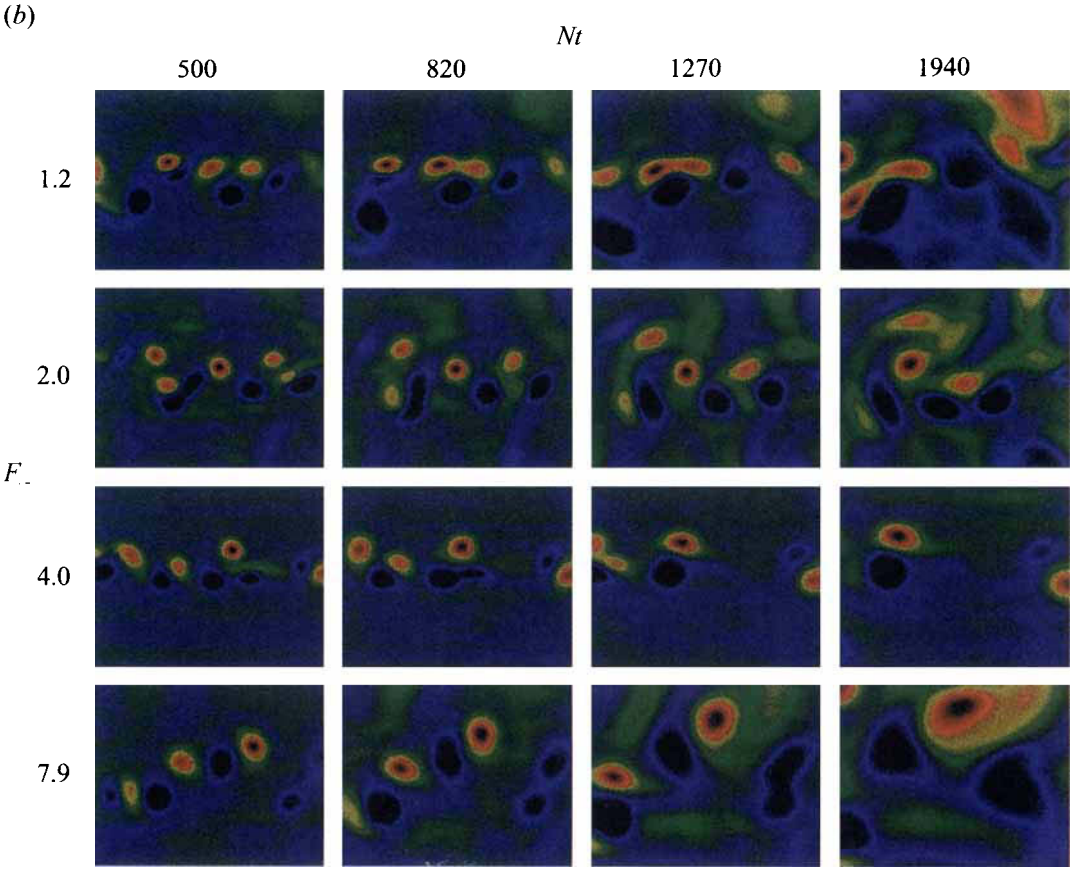

FIGURE 7. $\omega_z(F, Nt)$ for $Re \simeq 5 \times 10^3$. (*a*) $Nt \in [45, 245]$; (*b*) $Nt \in [500, 1940]$. Data from camera W.

will underpin much of the following discussion, is immediately established: *the vortex wake exhibits a high degree of order, as quasi-periodic arrays of vortices can be seen at all F, and for long times.*

The degree of regularity might be expected to depend on *Re*, and figure 8 shows $\omega_z(x, y, Nt)$ for four different values of *Re*, at $F = 10$. In figure 8(*a*), one can make a qualitative distinction between the two top rows for $Re < 5 \times 10^3$, and the lower two rows for $Re > 5 \times 10^3$. It is at the *higher Re* that the more regular-shaped patches of vertical vorticity emerge, and the lower *Re* wakes have a more fragmented, non-smooth appearance. Most of this qualitative difference has disappeared at the later times in figure 8(*b*).

Some caution is required here, as the top and bottom rows correspond to spheres of different diameters, and figures 7 and 8 have not been rescaled according to the sphere size (we prefer instead to retain the same sampling resolution:image size ratio). More seriously, one might suspect that confinement effects could be responsible for the apparent *Re*-dependence, since D/H changes. Yet this is not consistent with the noted *F*-independence of the R10 series in figure 7, where *D* also varies by a factor of two (table 1).

Instead, the second major qualitative result seems established: *there appears to be a minimum Re for the generation of coherent and stable vortex patches.* The patches emerge from initially turbulent conditions, and since this seems to depend on *Re*,

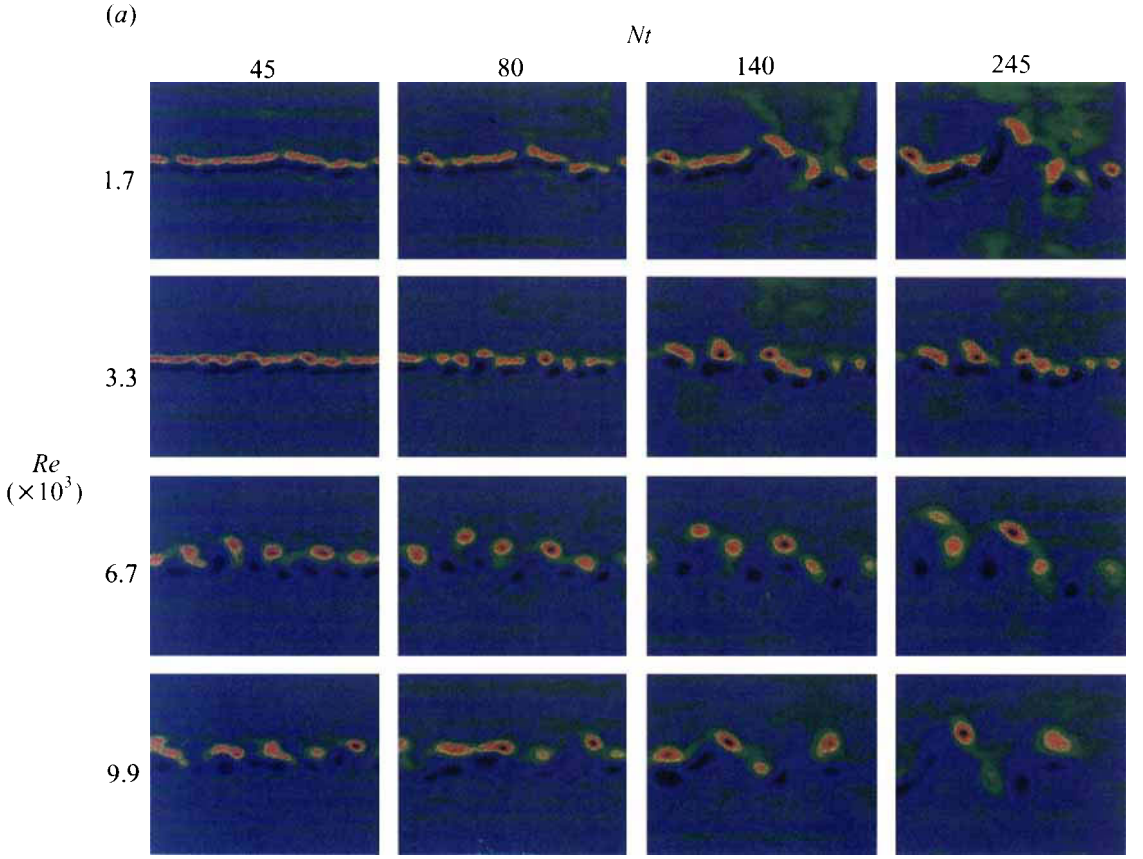

FIGURE 8 (*a*). For caption see facing page.

independent of F at sufficiently high Re, a requirement for a minimum range of scales in the initial turbulent wake is implicated. If these conditions are met, then the wake structure seems rather stable and long lived, spreading laterally quite slowly. Although one can interpret certain of the vortex structures in the wakes at moderate times, $Nt = O(10^2)$, as vortex pairs, or couples, they do not appear to separate and propagate away from their spatial origin, remaining instead close to the centreline at $y = 0$.

The qualitative results on the structure of $\omega_z(x, y)$ can be placed on a firmer, quantitative footing, where mean profile and turbulence quantities can be measured and compared with turbulent wakes in homogeneous fluids.

3.3. *Self-similarity in stratified wakes*

3.3.1. *Mean profiles and comparison with unstratified wakes*

Spedding *et al.* (1996) gave some simple scaling arguments that, when combined with empirical coefficients from three-dimensional turbulent wake studies, showed that values of $F \geqslant 3$ are required for turbulence to be active on all scales in a stratified wake, noting that this result was also consistent with results in CH93*a,b*. It is interesting to note, however, that qualitatively-speaking there is no apparent F-dependence in figure 7.

In any event, given sufficiently high initial values of Re and F (determined by the velocity and length scales of the moving body), it would be reasonable to predict that

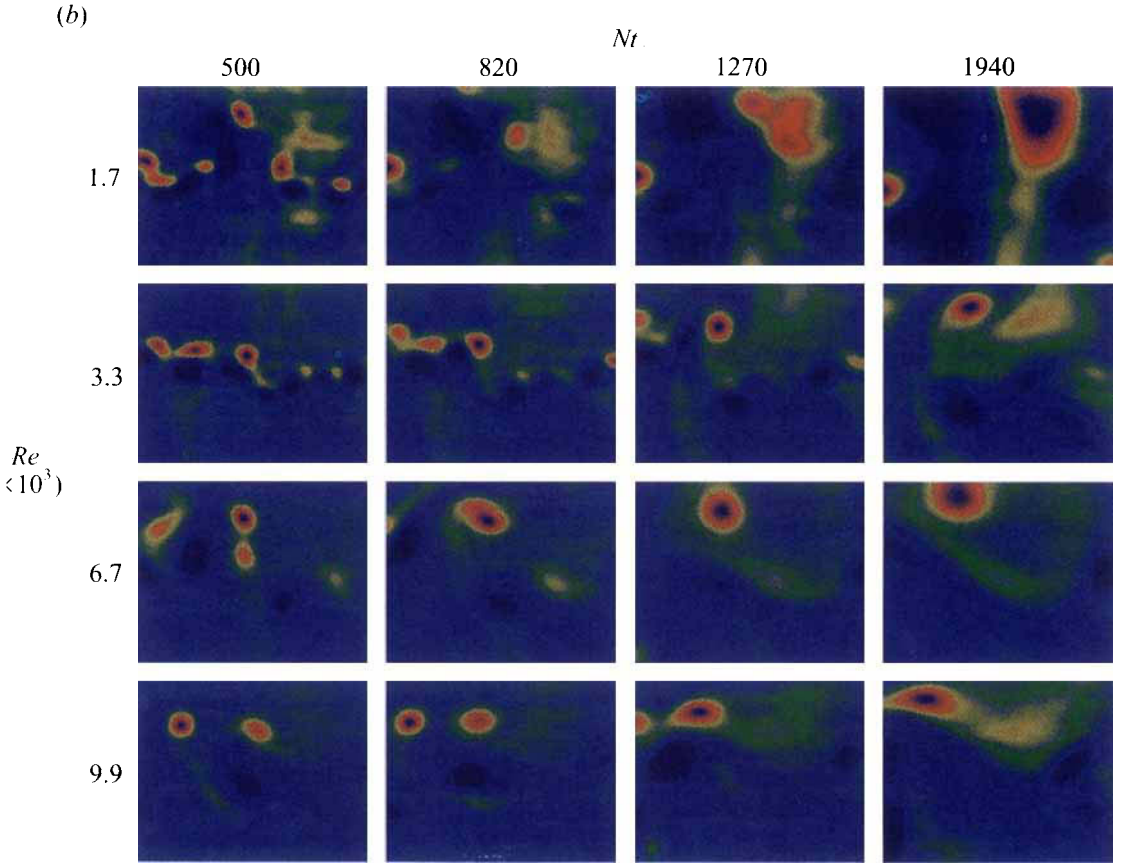

FIGURE 8. $\omega_z(Re, Nt)$ for $F = 10$. (*a*) $Nt \in [45, 245]$; (*b*) $Nt \in [500, 1940]$. Data from camera W.

a stratified wake would evolve as a three-dimensional wake in a homogeneous fluid, departing from this behaviour at some point, when local Re and F values drop below a critical value. There are three notable experimental studies of turbulent sphere wakes in homgeneous fluids, by Gibson, Chen & Lin (1968), Uberoi & Freymuth (1970) and Bevilaqua & Lykoudis (1978), and quantitative comparisons can be made with their measurements.

Indeed, figure 9 shows that profiles of ΔX-averaged streamwise velocities, $U_X(y)$, collapse quite well when rescaled by the local mean wake width, L_W, and the X-averaged peak value, U_0. The particular example is for $Re \simeq 10^4$, $F = 7.6$, and self-similar forms can be found up until $Nt = 633$ ($x/D = 2408$), which is the last one included. Later, the shape begins to differ substantially, and there are difficulties associated with making a statistical measurement in a domain that contains fewer vortices, located further from the centreline.

The profiles have a Gaussian shape, except for the tails of the distribution, which are usually negative. This is due to the comparatively unvarying y-location of the wake vortices; since they are quite closely aligned at some average y-location, the mean induced velocity does not average to zero, but to a non-zero mean, opposite in sign to the wake defect velocity. Such negative tails can also be observed in the three-dimensional sphere wakes for $x/D < 1.4$ (Bevilaqua & Lykoudis 1978), but in the stratified case, they remain for much larger equivalent x/D.

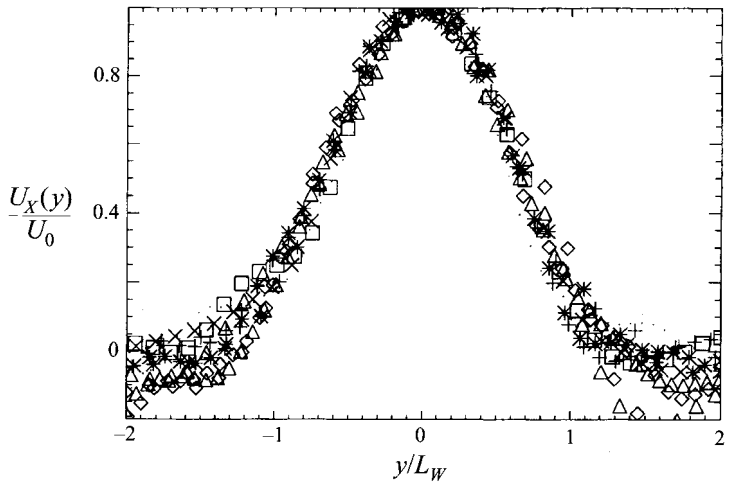

FIGURE 9. Self-similar scaling of $U_X(y)$ for 9 values of Nt from 33 to 633 for $Re \simeq 10^4$, $F = 7.6$.

Fitting profiles such as figure 9 with Gaussians of the form,

$$U_X(y) = U_0 e^{-(y^2/2L_\sigma^2)},$$

allows local length and velocity scales, L_σ and U_0, to be defined. L_σ serves a similar function to L_W, but is contingent on the shape of $U_X(y)$. Self-similarity implies power law behaviour of these scales as

$$\left(\frac{L_\sigma}{D}\right) \simeq B_0 \left(\frac{x}{D}\right)^{B_1}, \tag{3.1}$$

and

$$\left(\frac{U_0}{U}\right) \simeq C_0 \left(\frac{x}{D}\right)^{C_1}. \tag{3.2}$$

For three-dimensional wakes in a homogeneous fluid, with $Re \in [8.6 \times 10^3, 8 \times 10^4]$, Gibson *et al.* (1968), Uberoik & Freymuth (1970) and Bevilaqua & Lykoudis (1978) found that the exponents B_1 and C_1 for L/D and U_0/U, respectively were approximately $1/3$ and $-2/3$ (Gibson *et al.* actually found $C_1 \simeq -0.85$).

Figure 10(*a,b*) shows the evolution of L_σ and U_0 with x/D, for a collection of data at $Re \in [5 \times 10^3, 1 \times 10^4]$ and $F \in [1, 15]$ (the R5 and R10 series), where the elapsed time, t, is converted to an equivalent downstream distance, $x/D = Ut/D$. In figure 10(*a*), the wake width follows a $1/3$ power law quite closely, although some variation in offset with F can be noted, where the lower-F curves lie further beneath the three-dimensional result. This is unexpected, as the usual notion is that growth in turbulent patches in a stable stratification is inhibited in the vertical, and correspondingly increased in the horizontal (cf. Flór, Fernando & van Heijst (1994), Fernando, van Heijst & Fonseka (1994) for two-layer and linear stratifications, Lin & Pao (1979) for self-propelled, slender body wakes). According to figure 10(*a*), the stronger the stratification, the narrower the wake. Any attempted extrapolation (in t or F), or generalization (to other geometries, momentumless wakes) of this result would best be made with extreme caution, first because horizontal spreading rates depend on the degree of mixing in the near wake (which is low here), and second, because a simple power law behaviour observed in the late-wake centreplane does not imply that the

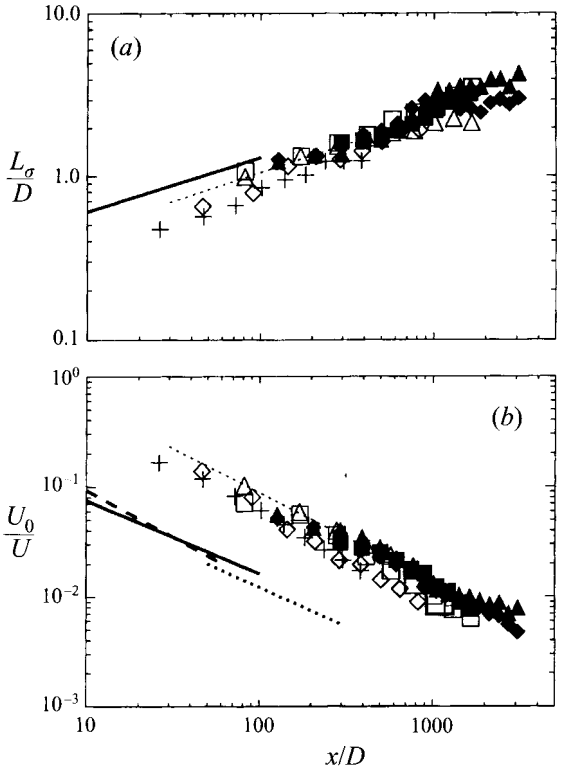

FIGURE 10. (*a*) Normalized wake width, L_σ/D, as a function of downstream distance, x/D for R5 (figure 7), where $Re \approx 5 \times 10^3$, and $F = \{1.2, 2.0, 4.0, 7.9\}$ for symbols $\{+, \diamond, \triangle, \square\}$, and for R10, where $Re \approx 10^4$, and $F = \{7.6, 9.8, 14.7\}$ for the filled symbols $\{\blacklozenge, \blacktriangle, \blacksquare\}$. The solid line is from Bevilaqua & Lykoudis (1978). The dotted line is a least-squares fit to the R5 and R10 data, calculated over $x/D = [100, 1000]$. (*b*) U_0/U *vs.* x/D. Symbols as in (*a*). The thick lines are from Bevilaqua & Lykoudis (1978) (solid line), Gibson *et al.* (1968) (dashed) and Uberoi & Freymuth (1970) (dotted). The thin dotted line is a least-squares fit, as above, and the large square is an estimate from CH93*a*.

dynamics are always describable this way, or that the dynamics truly resemble a three-dimensional homogeneous wake. The measured power laws are certainly the result of quite complex and differing dynamics in the horizontal and vertical directions. Further remarks are postponed until the discussion section (esp. §§4.1,4.2).

Further notable similarities and differences with three-dimensional turbulent wakes can be seen in figure 10(*b*), which shows that while the mean decay rate in U_0/U is well predicted by a $-2/3$ (or -0.85, Gibson *et al.* 1968) power law, at any given x/D the peak defect velocity is about eight times the value expected in an unstratified wake. The large square at $x/D \approx 1000$ shows the only other data that can be extracted from the literature, estimated from a figure in CH93*a*, and it falls close to the fitted line. CH93*a* also reported two values for the maximum turbulent velocity at $z/R = 0$, $Nt = 750$, of $u_{max} \simeq 0.1$ cm s^{-1} at $F = 3$, and $u_{max} \simeq 0.15$ cm s^{-1} at $F = 5$. This corresponds to ratios of $u_{max}/U = 0.013$ and 0.012 for $F = 3$ and 5, respectively, and so the points would lie towards the top of the range of values of U_0/U in figure 10(*b*) for the appropriate x/D, just as one might expect, as $u_{max} \geqslant U_0$.

In both cases, the dotted line is the mean least-squares fit through the data calculated for the range $x/D \in [100, 1000]$. The mean slopes of 0.35 and -0.80 do

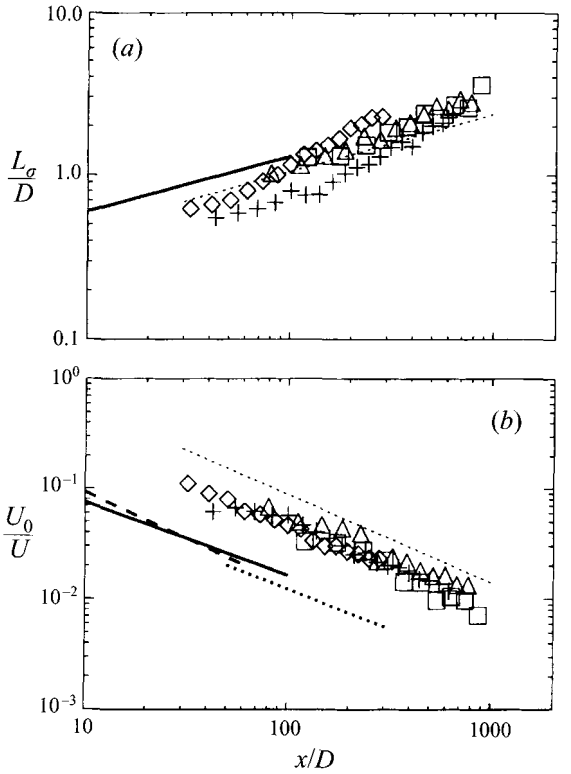

FIGURE 11. (*a*) L_σ/D and (*b*) U_0/U *vs.* (x/D) for R2 series. $Re \approx 1730$ and $F = \{1.2, 1.6, 3.9, 10\}$ for symbols $\{+, \diamond, \triangle, \square\}$. Dotted lines are the least-squares estimates from figure 10. Bold lines from the literature are also as drawn in that figure.

not differ significantly from the unstratified wake results, shown in thick lines. The higher-Re data (R10, filled symbols) do not differ significantly from the lower-Re values (R5, open symbols), either in slope or offset. The R10 series, for $F \in [7.9, 14.7]$, agrees well with the higher-F values in R5 for L_σ/D.

The data do not collapse at all Re, however, and figure 11 shows an example for the R2 series, where $Re \approx 1730$, and F varies from 1.2 to 10. The wake width increases faster than at higher Re, and the mean slope of 0.51 differs significantly from the high-Re (and hence, also, the unstratified literature) results. It is in fact closer to the value expected from a two-dimensional plane wake. There are indications that the exponent is sensitive to the value of F. The mean defect velocity is consistently lower in magnitude, independent of F. It is much harder to claim either self-similarity, or simple power law behaviour in the low-Re data, as the Gaussian fit to the mean $U_X(y)$ profiles is considerably less convincing. This, together with the slightly higher L_σ/D values and the reduced U_0/U, are symptoms of the less regular, more fragmentary wake geometry previously noted in figure 8.

The constants in equations (3.1) and (3.2) can be estimated from least-squares fits to the data in figures 10 and 11 and are shown in table 2. It is not a very precise measurement, and so exact numerical values should not be inferred. The individual values given for the R5 case, for example, differ slightly from those quoted in SBF96 (because the fit covers a different, more limited range of x/D), but the mean values are close. Based on the preceding discussion and observations on figures 10 and 11,

Series	Exp.	L_σ/D B_0	B_1 (1/3)	U_0/U C_0	C_1 (−2/3)
F10	F10.2	0.19	0.39	1.44	−0.77
	F10.3	0.40	0.25	2.95	−0.80
	F10.6	0.12	0.47	8.14	−0.94
	F10.10	0.22	0.34	1.38	−0.64
R2	R2.1	0.07	0.52	1.82	−0.78
	R2.2	0.06	0.64	1.46	−0.75
	R2.4	0.12	0.48	2.13	−0.77
	R2.8	0.21	0.38	1.07	−0.71
R5	R5.1	0.20	0.31	4.89	−0.95
	R5.2	0.23	0.32	3.14	−0.87
	R5.4	0.37	0.25	2.76	−0.75
	R5.8	0.14	0.43	9.11	−0.99
	mean	0.24	0.33	4.98	−0.89
	sd	0.10	0.08	2.91	0.11
R10	R10.8	0.17	0.40	1.16	−0.63
	R10.10	0.22	0.34	1.38	−0.64
	R10.15	0.34	0.27	0.85	−0.58
	mean	0.24	0.34	1.13	−0.62
	sd	0.09	0.07	0.27	0.03

TABLE 2. Constants for scaling of wake width, L_σ/D, and U_0/U with downstream distance, x/D, for tracks of constant F (F10), and constant Re (R2, R5, R10). The (1/3) and (−2/3) headers are predictions from three-dimensional turbulent wakes.

mean values are only given for the R5 and R10 series. The overall mean values are

$$B_0 = 0.2 \pm 0.1 \quad \text{and} \quad B_1 = 0.34 \pm 0.06,$$

and

$$C_0 = 2.7 \pm 1.9 \quad \text{and} \quad C_1 = -0.75 \pm 0.15.$$

Little significance can be attributed to the rather uncertain estimates of the multiplying constants B_0 and C_0, but it is quite clear that neither of the exponents, B_1, C_1 differ significantly from those expected, and measured experimentally in three-dimensional unstratified wakes. The accumulated evidence from data in the domain of figure 6 suggests that these values are Re-independent, and show no consistent variation with F for $Re \geqslant 4 - 5 \times 10^3$. As a limited test of this idea, three miscellaneous cases in the range $Re \in [5 \times 10^3, 2 \times 10^4]$ and $F \in [5, 30]$ are shown in figure 12. The empirical constants given above were those used to generate the thin dotted lines, which predict the data well in all cases, regardless of Re or F, up to $x/D \simeq 800$. It is quite notable that the three-dimensional unstratified results should give the correct power laws for the evolution of the stratified wakes at such large x/D. Also, presumably at some $F > 30$, the centreline velocity must decline to eventually match with the homogeneous fluid result, but the approximately order of magnitude increase appears to occur over quite a substantial range of high $\{Re, F\}$.

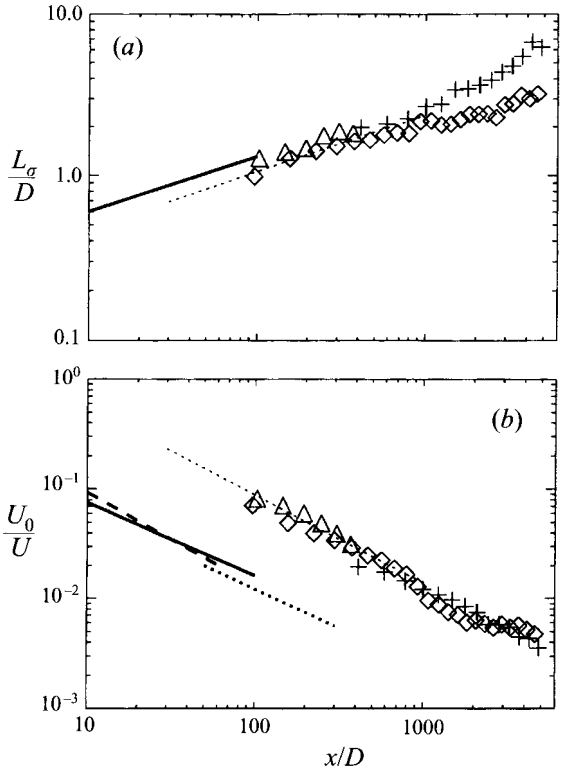

FIGURE 12. (*a*) L_σ/D and (*b*) U_0/U *vs.* (x/D) for selected $\{Re, F\}$ pairs: $\{5 \times 10^3, 30\}$, $\{1.3 \times 10^4, 5.8\}$ and $\{2.0 \times 10^4, 4.9\}$ for symbols $\{+, \diamond, \triangle\}$. Straight lines as in figure 10. The $\{+, \triangle\}$ experiments are for spheres with $D/H = \{0.08, 0.32\}$, respectively.

In turbulent free shear flows it is usual to define a virtual origin, x_0, by extrapolating backwards in the streamwise direction from some trend in characteristic length scale with x/D. Here, the origin of time in seconds was defined as the time at which the sphere passed through the centre of the measuring area, corrected for U. The chief effect of identifying and reducing data to a virtual origin extrapolated from $L_W/D(x/D)$ was to add scatter around this default point, partly because it was not immediately clear how to remove the F-dependence in $L_W/D(x/D)$ (e.g. figure 10*a*). The mean values did not differ systematically from the original estimate. Assigning x_0 to the effective (time-averaged) centre of the sphere is consistent with the remarks and procedure of Bevilaqua & Lykoudis (1978), and references therein. Errors in determining the wake origin would lead to departure from a simple power law at small x/D, and could add an effective offset to the measurements. However, there is no constant offset that could modify the agreement or difference between the stratified wake data and the values in the literature in one quantity, such as L_σ/D, without having the opposite effect on the other (e.g. U_0/U). The good agreement between $L_\sigma/D(x/D)$ and three-dimensional values when both Re and F are high lends further support to this strategy.

3.3.2. *Turbulence quantities*

Spedding *et al.* (1996) showed that various turbulence quantities in the late wake appeared to follow power laws for evolution with equivalent downstream distance, x/D, as would be predicted for three-dimensional turbulent wakes in a homogeneous

fluid. A dependence on F was noted, but not discussed further. While it is reasonable to expect three-dimensional scaling arguments to hold initially, at some time there must be a departure, when an Nt time scale is likely to be relevant, as stratification effects dominate. It is useful therefore to couch the scaling arguments in stratification parameters, and as a first estimate, the relationship $x/D = \frac{1}{2}FNt$ can simply be substituted into similarity forms whose physics are derived entirely from three-dimensional unstratified arguments. For example, consider the expected decay of the turbulent velocity fluctuation, q. In a self-preserving turbulent flow, the velocity fluctuations scale as mean flow quantities. Thus $q \sim U_0$, and so one expects

$$\frac{q}{U} \sim \left(\frac{x}{D}\right)^{-2/3}. \tag{3.3}$$

For three-dimensional wakes this was verified by Gibson *et al.* (1968), Uberoi & Freymuth (1970) and Bevilaqua & Lykoudis (1978), and the preceding result for C_1 gives good reason to expect a similar value in the stratified wakes also, at least initially. Substituting FNt for x/D, the scaling in terms of Nt is

$$\frac{q}{U}(F)^{2/3} \sim (Nt)^{-2/3}. \tag{3.4}$$

The vorticity depends only on local length and velocity scales, $\omega \sim u/L$, and since the relationships, $L \sim x/D^{1/3}$ and $u \sim x/D^{-2/3}$, although originally derived and measured for three-dimensional turbulent wakes, appear to hold also for unstratified wakes (constants B_1 and C_1 above), we have

$$\left(\frac{\omega}{U/D}\right) F \sim (Nt)^{-1}. \tag{3.5}$$

Similarly, since $\epsilon \sim u^3/L$,

$$\frac{\langle\epsilon\rangle}{U^3/D}(F)^{7/3} \sim (Nt)^{-7/3}. \tag{3.6}$$

The scaling relations in (3.4)–(3.6) incorporate the presumed dependence on F, and are independent of Re, for sufficiently large Re. The quantities $E^{1/2}$, $W^{1/2}$ and S defined in §2.3.8 can be used as measures of wake-averaged q, ω_z and ϵ_z to test these predictions.

Figure 13 shows the remarkable collapse of the data onto lines of constant slope, over a reasonable range of Nt, for the rescaled q, ω_z and ϵ_z. The experimentally derived slopes of the q and ω_z decay are not significantly different from the predicted slope. It is rather extraordinary that an essentially (slightly) modified three-dimensional argument nevertheless predicts the data quite well, even at very late times ($Nt \approx 500$) in terms of the known anisotropy of the velocity field. Vertical velocities are extremely small, and almost all the energy is contained in the quasi-two-dimensional vortex motions. The exception here appears to be in the dissipation rates, which collapse onto a line that has significantly different slope than the $-7/3$ prediction. Since $\Delta_z = -\partial w/\partial z$, then the contribution of $(\partial w/\partial z)^2$ to the total dissipation can also be estimated. Although at intermediate times the measured Δ_z is contaminated by reflected internal waves, order of magnitude estimates for $\epsilon_z/\nu(\Delta_z)^2$ are $\geqslant 10$ for $Nt < 200$, and $\geqslant 100$ for $Nt > 1000$, and so this term is not responsible for significant fractions of the total kinetic energy dissipation, nor for its overall decay rate.

The behaviour out beyond $Nt = 1000$ up until $Nt \approx 3000$ can be seen in figure 14, which is from the same series of experiments, but from the wide-angle-lens camera.

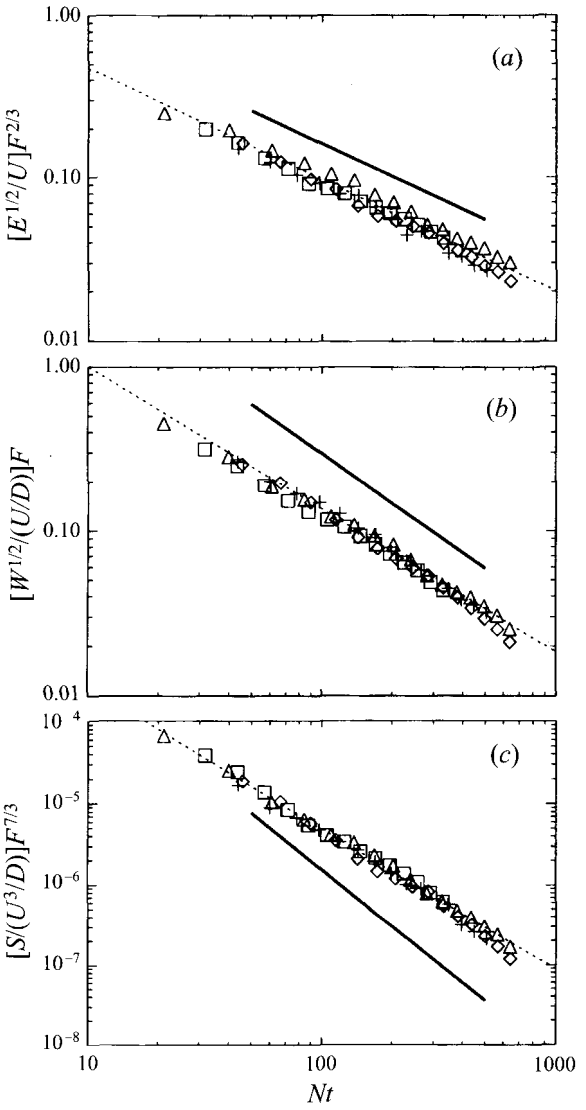

FIGURE 13. The normalized fluctuation velocity (*a*), vorticity magnitude (*b*), and energy dissipation rate (*c*) *vs.* Nt for R5. Symbols as in figure 10. The thick solid line shows the predicted decay rate, and is drawn over the range of Nt for which a least-squares fit was made, which is shown as a dotted line spanning the whole range of Nt (this makes departures from the line more evident).

Where the range of Nt overlaps with figure 14, the agreement between the two can be verified, and slopes measured over similar ranges of Nt are identical, within experimental uncertainty. The departure from the power law decay, just becoming noticeable in figure 13, is more evident, and continues consistently at later times. The point at which this happens is around Nt = 600–800, and does not seem to vary with F. The roll-off at high Nt is more noticeable in the quantities involving spatial derivatives, ω_z and ϵ_z (figure 14*b*,*c*).

Based on results from mean profiles, one might expect the similarity of the turbulence measures to hold only for sufficiently high Re, and this is so. Figure 15 shows the same measurement for the F10 series. The collapse of the data is less successful, and the two lowest-Re cases, where Re = 1685 and 3300, differ both from the two

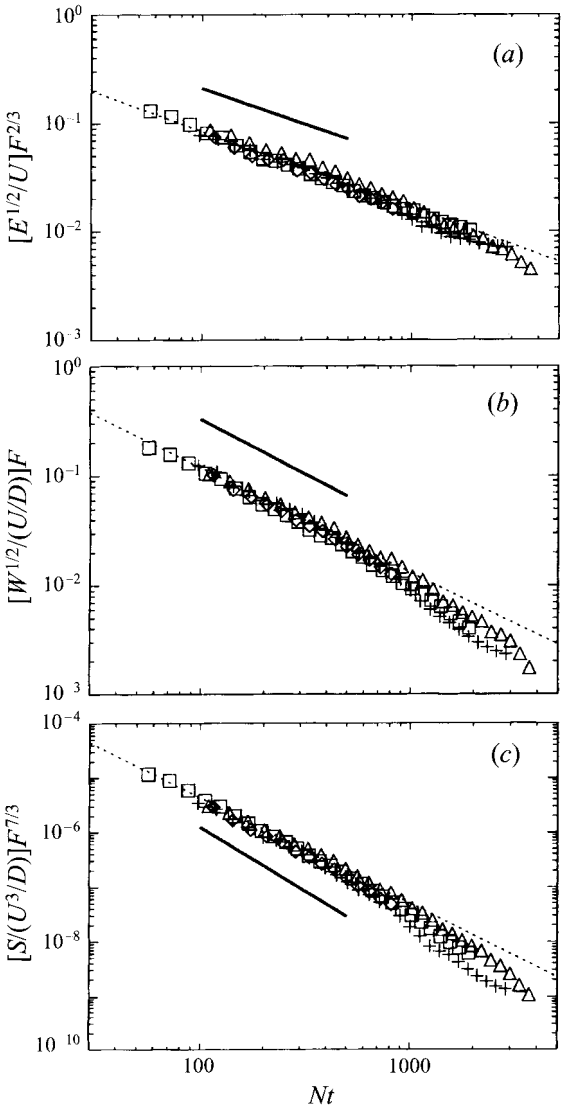

FIGURE 14. Same physical experiment as figure 13, but data acquired with the wide-angle lens. Plotting conventions as in previous figure.

higher-Re cases ($Re = 6715$ and 9880), and from the R5 data whose least-squares fit is given by the dotted line. The high-Re curves do not differ significantly from this line. The dissipation curves do not appear to vary in a simple way with Re. Overall, however, it appears that the sphere wake measurements do not collapse in all the quantities measured here unless $Re \geqslant 4$–5×10^3.

There is potential for misinterpretation of variations in Re because the low-Re runs involve spheres with half the diameter of the higher-Re cases. Consequently errors due to limited spatial resolution that will be most prominent at early Nt might be expected to vary in severity consistently with Re, particularly since figure 15 is derived from the wide-angle camera, and so has the coarsest resolution. However, the fine-scale data reproduce all these trends very closely, and all data that overlap in Nt are thus confirmed. Furthermore, no such explanations can apply to the measurable

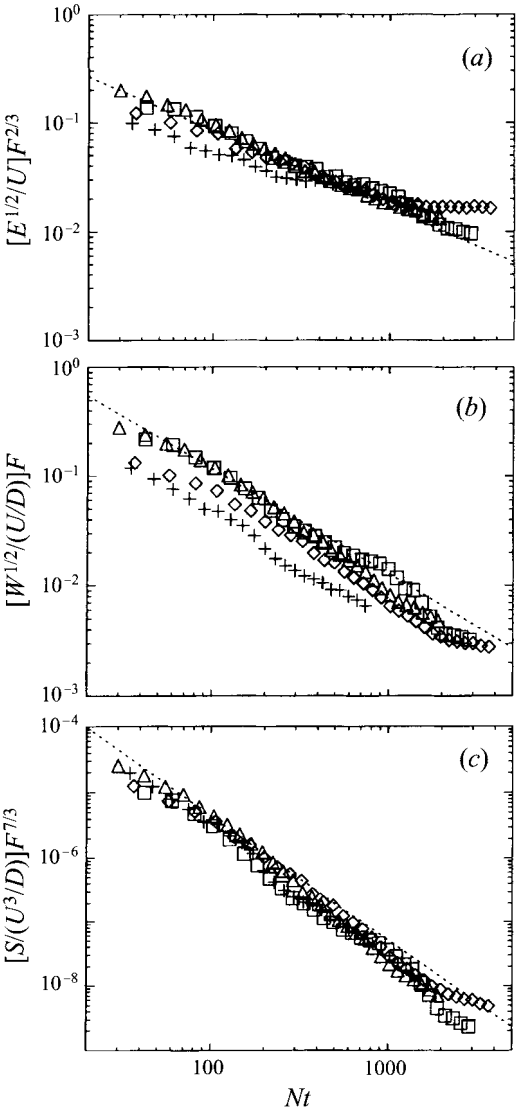

FIGURE 15. Normalized fluctuation velocity (*a*), vorticity magnitude (*b*), and energy dissipation rate (*c*) *vs.* Nt for F10, where $Re = \{1685, 3300, 6715, 9880\}$ for symbols $\{+, \diamond, \triangle, \square\}$. The thin dotted line is the mean of the R5 and R10 series.

differences at much later times ($Nt > 100$) when the dominant scales of motion are very large compared with either mesh.

There are eleven experiments in which Re is high enough that the empirical constants determining the decay rates of the turbulence quantities may be averaged together, and the overall result is given in table 3. *Mirabile dictu*, the decay rates of the velocity fluctuations and of the vorticity magnitude do not differ significantly from the original predictions based on an extrapolation of three-dimensional turbulence scaling out into stratified data. It is far from clear why this is so, and even less clear why it holds for such late times. The rescaled dissipation rate decays at a significantly lower rate than the three-dimensional arguments would indicate. Further interpretation of these points will be postponed to the discussion section.

LHS	C		α	
	mean	sd	mean	sd
$\left(\frac{E^{1/2}}{U}\right) F^{2/3}$	2.3	0.4	−0.71	0.05
$\left(\frac{W^{1/2}}{U/D}\right) F$	8.6	2.4	−0.91	0.07
$\left(\frac{S}{U^3/D}\right) F^{7/3}$	0.023	0.014	−1.83	0.14

TABLE 3. Scaling in equations (3.4)–(3.6), represented in general form, LHS $\simeq C(Nt)^{\alpha}$. C and α are mean values from 11 different $\{Re, F\}$ pairs for $Re \geqslant 5 \times 10^3$.

3.3.3. *Practical limits in wake detection*

A cursory inspection of figures 7 and 8 shows that coherent wake structures are observable in the the centreplane even at very large Nt, and it is of some practical interest to know for how long these wake signatures remain detectable, above the background noise. Figure 16 compares the time evolution of the inner wake and outer ambient (as defined in figure 5) averaged velocity fluctuations (figure 16*a*) and vorticity fluctuations (figure 16*b*). In both cases, a substantial contribution to the ambient component actually comes from the edges of the wake region, outside the cutoff point at $0.2U_0$, reducing the signal:noise ratio by a factor of ten or more. However, the wake is clearly distinguishable by its higher mean values of fluctuating velocity and vorticity, up until $Nt \approx 2000$. In and around the ocean pycnocline, $N \approx 2 \times 10^{-3}$, and so $t_{obs} \approx 10^6$ s, or around 12 days. Although the result can be qualified by reminders that real wakes do not live in quiet ambient oceans, and that a surface signature must propagate first through an upper mixed layer, it is also true that t_{obs} was given above for averaged quantities, whose spatial distribution, or *pattern*, may be yet easier to extract.

The following sections examine the wake geometry in more detail.

3.4. *Vortex patch spacing, Strouhal number*

The streamwise separation distance, λ_x, between neighbouring vortices of the same sign was measured for as many time steps as there were judged to be a sufficient number of vortices for statistical validity, and figure 17 shows the effect of variations in F and Re on this measure, expressed as a Strouhal number, $St \equiv D/\lambda_x$.

The mean spacing, $\langle \lambda_x \rangle$, was measured in two ways, both of which are shown in figure 17. The simpler method is to manually identify successive vortices in the $\omega_z(x, y)$ fields at each Nt and to ensemble average the result. The procedure is computer-assisted so that the initial peak location, performed by eye, is refined with a two-dimensional interpolating fit, and certain other statistical criteria can be checked on the structure before computing a streamwise separation. The symbols mark the mean St value at each Nt, computed from these $\langle \lambda_x \rangle$. Alternatively, a localized and directional-specific spectral measurement on the same data should give the same result. A two-dimensional wavelet transform using the wavelet function *Morlet2D* (the properties of this, and other two-dimensional wavelet functions for data analysis are described in detail in Dallard & Spedding 1993) was performed. The wavelet function is direction-specific and is oriented at 0° so that resonance occurs only with

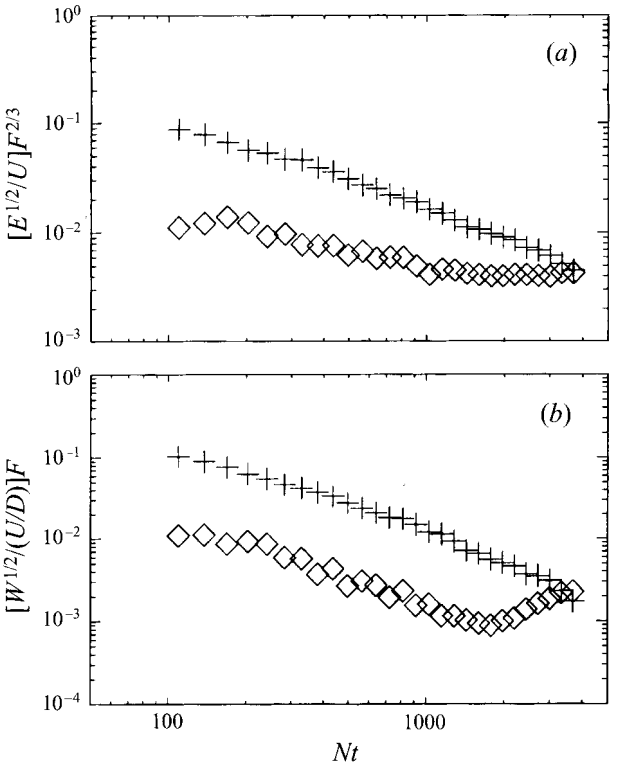

FIGURE 16. Normalized velocity (*a*) and vorticity (*b*) fluctuations for the wake region (+) and the outer ambient fluid (◇). The separation of outer from inner regions becomes increasingly difficult at $Nt > 2000$. The amplitude of the fluctuations in the outer region is artificially elevated by leakage from the finite energy wake cutoff criterion.

wavevectors aligned close to the x-direction ($k_y \approx 0$). The local wake width, L_W, defined previously, is used to define the spatial extent of a region in which the most dominant length scale is found by locating the centroid (in wavelet scale, a) of the modulus of the wavelet transform in this domain. Least-squares power law fits to the wavelet-derived measure of $\langle \lambda_x \rangle$ are shown with continuous lines in figure 17. The agreement with the manual method is excellent.

St steadily decreases with time, mainly through pairing of like-signed vortices, as can readily be observed in figures 7 and 8. The change in St is thus a measure of the rate at which pairing occurs. It also gives rise to the slightly stepwise changes in $St(Nt)$ in the hand-counted data of figure 17(*a*), as pairings occur at similar time steps across the whole field. The wavelet result tends to average out this effect.

The decay of St with Nt appears to be independent of F, although the absolute value of St depends on F over the whole range of $F \in [1.2, 8]$. CH93*b* and Bonneton *et al.* (1995) described the emergence of the collapsed spiral mode in the near wake at $F \approx 3$, where $St = 0.175$, and no variation with further increase in F. The horizontal lines in figure 17(*a–c*) are drawn at this value of St. Note that there is a clear F-dependence up until $F = 8$, and that while the spiral mode may dominate near-wake velocity fluctuations, there is no evidence that it has any special significance in determining the far-wake spacing. For $F > 2$, initial wake spacings are quite close to $St = 0.175$, as previously noted for $F = 4$ in Spedding *et al.* (1996).

Figure 17(*b,c*) shows that $St(Nt)$ is not particularly sensitive to changes in Re,

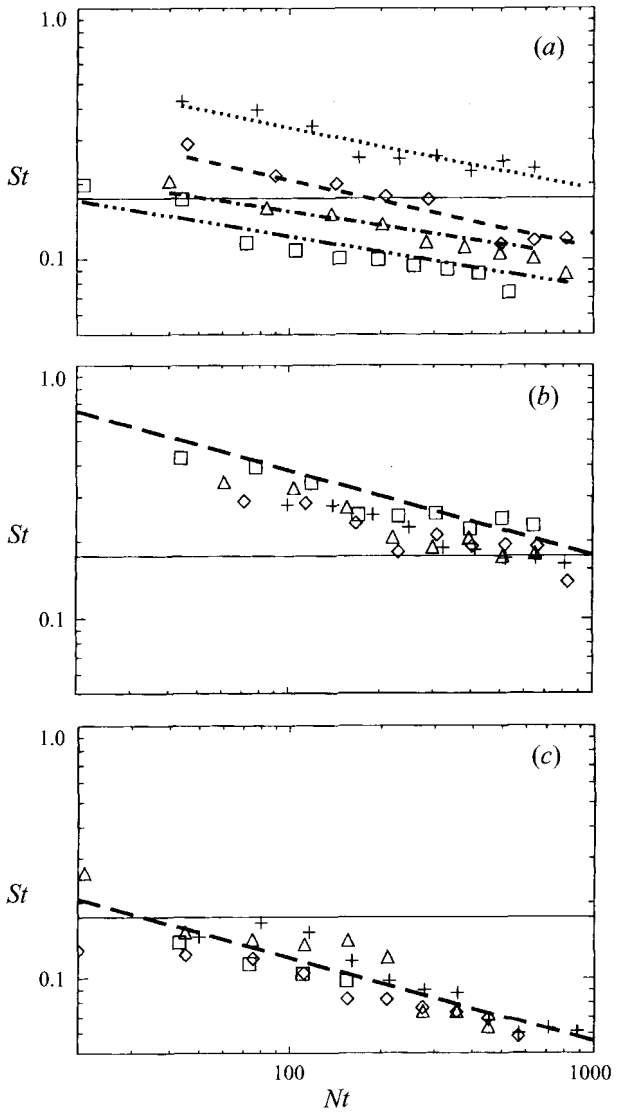

FIGURE 17. Wake Strouhal number, St, *vs.* Nt for R5 (*a*), F1 (*b*), and F10 (*c*). The symbols $\{+, \diamond, \triangle, \square\}$ denote $F = \{1.2, 2.0, 4.0, 7.9\}$, $Re = \{1216, 1558, 2700, 4877\}$ and $Re = \{1685, 3300, 6715, 9880\}$ for (*a*), (*b*) and (*c*) respectively. The straight lines are power law fits to independent measurements of St from wavelet transforms, as explained in the text. The long-dashed lines in (*b*) and (*c*) are averages over all Re in that series. The continuous, horizontal lines for $St = 0.175$ correspond to the expected value for the spiral instability mode.

for $F = 1.2$ and $F = 10$, although there is some scatter in the symbols, mostly at lower Re. The wavelet curve and the symbols do not agree so well for the F1 series (figure 17*b*). This is likely to be because when both Re and F are low, it is difficult to discern small-amplitude fluctuations in the mean vorticity profile, and the manual count probably overestimates the true wake spacing. When either F or Re is increased, the problem disappears, and agreement is once again good (the squares are the same data as the crosses in figure 17*a*). The absolute value of St varies with the different values of F in figure 17(*b*,*c*) as one would expect from the trend in figure 17(*a*). The decay rates do not vary measurably with either Re or F.

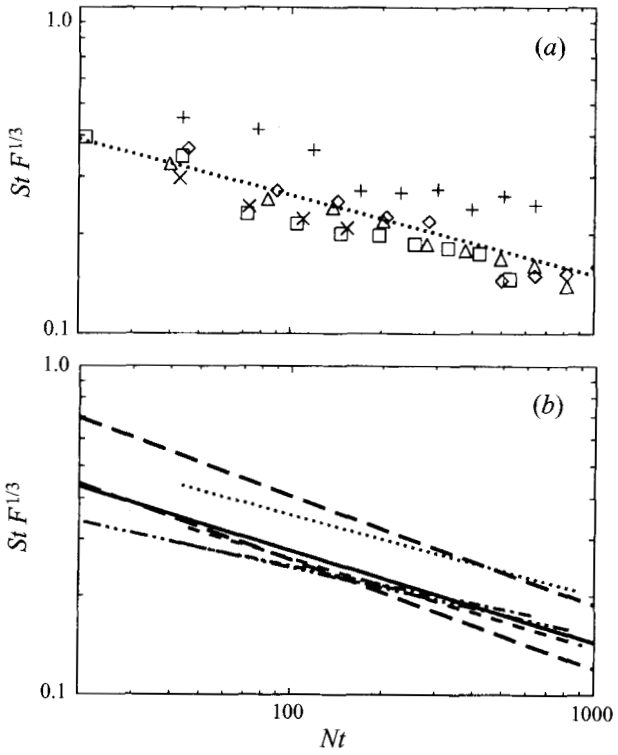

FIGURE 18. Rescaled Strouhal number, $StF^{1/3}$ *vs.* Nt. (*a*) Manually estimated wake spacing, where $Re \geqslant 5 \times 10^3$ and $F = \{1.2, 2.0, 4.0, 7.9, 10.0\}$ for symbols $\{+, \diamond, \triangle, \square, \times\}$. The dotted line is the mean value of separate least-squares fits through all the data but for the lowest $F = 1.2$, which does not collapse. (*b*) Wavelet transform-derived results from figure 17(*a–c*), retaining the same line types; of the two long-dashed lines, the F1 series is the uppermost. The solid line is a mean of all the individual fits for $F \geqslant 2$.

Suppose $\lambda_x \sim L_W$, then substituting the relation $x/D \simeq FNt$ into equation (3.1) and retaining the 1/3 exponent as suggested by the results in §3.3.1, we arrive at an equation for $\lambda_x(Nt)$ that incorporates a predicted F dependence as

$$\frac{\lambda_x}{D} \sim \frac{L_W}{D} \sim \left(\frac{U}{ND}\right)^{1/3} Nt^{1/3}. \tag{3.7}$$

Hence, $St \sim D/\lambda_x$ should vary as

$$St \sim F^{-1/3} Nt^{-1/3}. \tag{3.8}$$

Figure 18 shows that the rescaling is quite successful in collapsing the data for $2 \leqslant F \leqslant 10$. The $F = 1.2$ curve, for both hand-counted (figure 18*a*) and wavelet-based (figure 18*b*), lies significantly away from the rest of the data. The non-collapse is the first sign of the possible existence of a transitional F value in the current data, but its implied value lies well below the expected 3–6 range. Least-squares fits to the hand-counted and wavelet-based collapsed data (shown as dotted and solid lines in figure 18(*a,b*), respectively), give a multiplying constant, and exponent for equation (3.8) that do not differ significantly from 1, and $-1/3$, respectively.

CH93*b* and Bonneton *et al.* (1995) report $St \sim F^{-3/2}$ for $F \leqslant 3$, but no systematic dependence of St on F at higher F. The low Froude number behaviour observed

here is therefore more consistent with their low-F result, in that the magnitude of the exponent would increase in the appropriate direction. The higher-F values still show a (predicted) F-dependence, but it is always for a relatively late wake flow, not necessarily directly comparable with the near-wake, hot-film results. At high enough F, the spiral mode may determine the earliest detectable coherent streamwise wavenumber. Afterwards, the wake kinetic energy decays, local Froude numbers are low, and the spacing is determined by nonlinear vortex pairing mechanisms, and the $St(Nt)$ decay rate no longer depends on F or Re. Nevertheless, some memory of the initial Froude number is retained through the absolute value of St. By contrast, there is no remnant of the differing Re over this Re range.

3.5. *Local $\{Re, F\}$ in stratified wakes*

In the previous section, wavelet transforms were used to measure local length scales in the wake. Since the fluctuating velocity distribution, $q(x, y)$, is also known, this suggests the use of these scales to define local $Re(x, y)$ (see Farge 1992) and $F(x, y)$ fields. Denoting by $\tilde{\omega}_z(a, \boldsymbol{b})$ the wavelet transform at scale, a, and position $\boldsymbol{b}$, of the vertical vorticity field, then at each spatial location, (x, y) (= $\boldsymbol{b}$ here), a characteristic scale, l_X, can be defined as the scale at which $|\tilde{\omega}_z(a, \boldsymbol{b})|$ has its maximum value. Now, the local Reynolds number can be defined as

$$Re_X(x, y) \equiv \frac{q(x, y) l_X(x, y)}{\nu}, \tag{3.9}$$

and its spatially averaged value is computed from all locations at which the transform modulus exceeds some minimum threshold, T,

$$\langle Re \rangle = \langle Re_X(x, y) \rangle_{|\tilde{\omega}_z(a,\boldsymbol{b})|>T}. \tag{3.10}$$

Similarly, a local Froude number can be defined as

$$F_X(x, y) \equiv \frac{q(x, y)}{N l_X(x, y)}, \tag{3.11}$$

and the corresponding average value is

$$\langle F \rangle = \langle F_X(x, y) \rangle_{|\tilde{\omega}_z(a,\boldsymbol{b})|>T}. \tag{3.12}$$

The X-subscripts (omitted for convenience in the wake-averaged values) refer to the fact that the length scales are computed from a direction-specific wavelet that selects wavevectors aligned in x. This is to avoid introducing the wake width itself as a non-independent length scale.

Figure 19 shows that at all times the spatial distributions of $Re_X(x, y)$ and $F_X(x, y)$ are roughly similar. This is because the dominant length scale, l_X, does not vary greatly across the wake, so the major fluctuating term in both quantities is just the velocity magnitude, q. Consequently, at later times, vortex core centres are marked by regions of very *low* Re and F. Otherwise, regions of higher Re and F where nonlinear inertial forces may be significant occur predominantly in the wake centre early on, and at the vortex peripheries at later times. There is no apparent accumulation of enstrophy in small scales at the vortex core centres.

The mean and maximum $\langle Re \rangle$ and $\langle F \rangle$ values are plotted *vs.* Nt in figure 20 for the R5 series. As one might expect, the local $\langle Re \rangle$ values are initially approximately equal (the initial Re is constant), and their decay rate also appears to be independent of F. The mean, and maximum values behave in the same way. Since the wake width, L_W, grows as $(x/D)^{1/3} \sim Nt^{1/3}$, while $q \sim Nt^{-2/3}$, then $\langle Re \rangle \sim l_X q$ might be expected

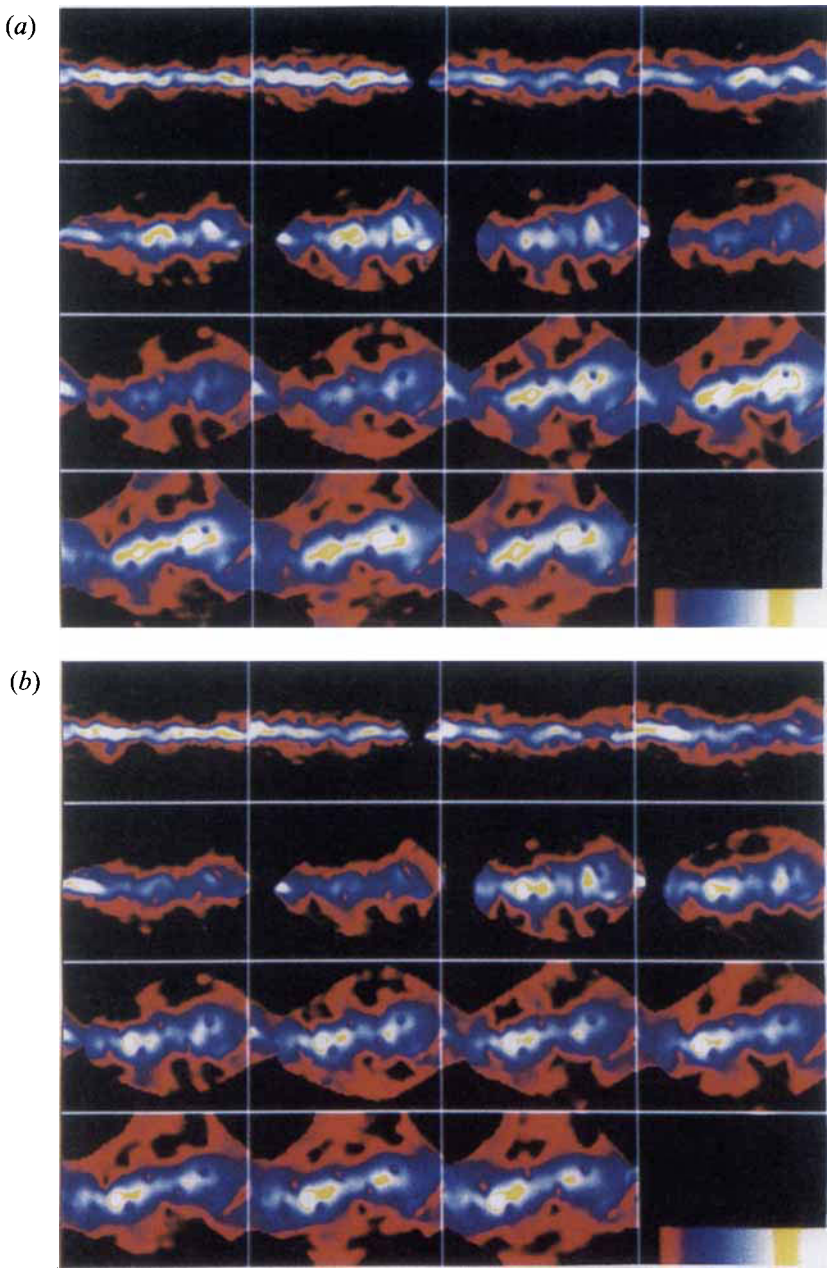

FIGURE 19. Local Reynolds number, $Re_X(x, y)$ (*a*), and local Froude number $F_X(x, y)$ (*b*), *vs.* Nt for initial values determined by the sphere geometry and velocity, $Re = 5286$, $F = 7.9$. Nt is in the range [21, 332], equivalent to $x/D = [82, 1305]$. At each (x, y) location, values are thresholded at 40% of the maximum value of the wavelet transform modulus at that Nt. At later times, characteristic length scales are larger, and the Re_X and F_X fields are truncated close to the edges of the data domain to remove artifacts due to the non-compact support of the wavelet function. The colour bar is rescaled to span the local range of Re_X and F_X at each Nt.

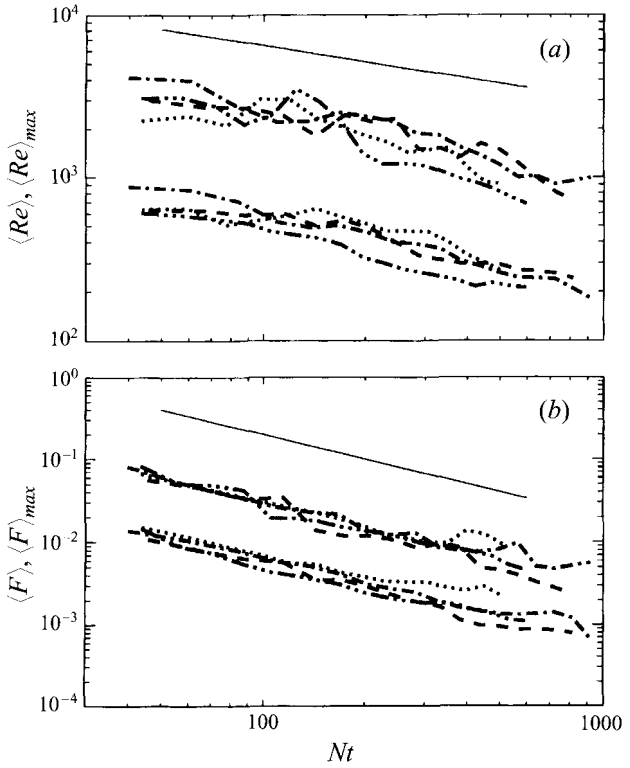

FIGURE 20. Average and maximum Reynolds number (*a*) and Froude number (*b*) from local wake length and velocity scales. Upper curves are the maximum value. The data are from R5 with $Re \approx 5 \times 10^3$ and F varying as $\{1.2, 2.0, 4.0, 7.9\}$ for lines {....., - - -, - - - -, - - - - - -}.

to scale as

$$\langle Re\rangle \sim Nt^{-1/3},$$

provided $l_X \sim L_W$. The solid line shows this to be a reasonable approximation of the measured decay rate. In figure 20(*b*) it is immediately apparent that $\langle F\rangle$ is always quite low, regardless of the initial F. The collapse of the curves provides a physical interpretation for the comparative independence of the mean profile and turbulence data of the initial value of F; since the *local* Froude number is always low, and not very sensitive to its initial value, buoyancy effects are always dominant in the evolution of the late wake. Reasoning as above, one may expect,

$$\langle F\rangle \sim Nt^{-1},$$

which again agrees well with the data. The mean and maximum curves differ by an order of magnitude in absolute value, giving an indication of the magnitude of the fluctuations about $\langle F\rangle$, but their slopes are identical.

Figure 21 shows the variation in $\langle Re\rangle(Nt)$ and $\langle F\rangle(Nt)$ with Re, for the F10 series. $\langle Re\rangle$ differs significantly in absolute value depending on its initial value, and this difference is measurable for long times. At the higher Re values, the slopes agree satisfactorily (insofar as a constant slope of any kind exists) with the previously noted $-1/3$ value. The slope itself varies with Re at lower Re, and in the lowest case (for initial $Re = 1685$) $\langle Re\rangle$ is approximately constant up to $Nt \approx 1000$. The collapse of the $\langle F\rangle(Nt)$ curves is less successful than for the R5 series, but the higher-Re cases

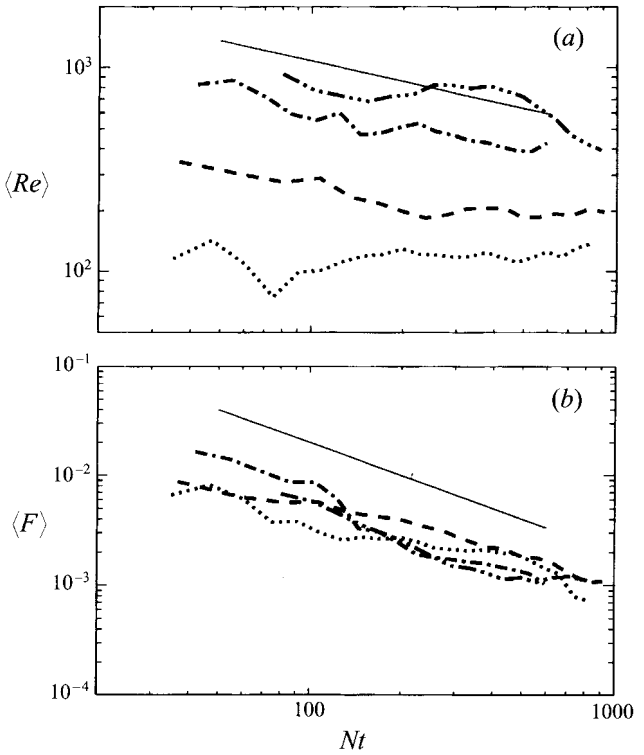

FIGURE 21. Variation in local $\langle Re \rangle$ (*a*), and $\langle F \rangle$ (*b*) with initial Re in F10. $Re = \{1685, 3300, 6715, 9880\}$ for lines {....., - - -, - . - . -, - . . . . . -}.

are quite well predicted by the Nt^{-1} relation given by the solid line, and consistent with the R5 data in figure 20(*b*).

3.6. *Vortex geometry and time evolution*

3.6.1. *General form of the vorticity distribution*

The time evolution and geometry of individual vortices can be measured once they have become separately identifiable coherent features. The time, Nt, at which that happens is not greatly sensitive to F (figure 7), but does vary with Re (figure 8). By selecting only those vortices that appear as distinct structures, some of the structural difference is lost since the basic shape is pre-selected, but one can still investigate the vorticity distribution of the selected structures for different Nt, F and Re and look for remaining similarities and differences.

At any given timestep, vortices were manually selected and a computer-generated bicubic spline was fit about the peak to give an interpolated (x, y) location for the maximum value, ω_0 (the z subscript will be omitted for clarity in this section). As in the wake width measurements, a characteristic length scale, l_ω, can be defined as the radial distance from the centre to where $\omega(r)$ falls to some fraction of the maximum value, set here to $0.2\omega_0$. We do not wish to measure deformations of the shape due to merging events, and when such occurrences noticeably distort the radial symmetry, either they are omitted entirely, or only transects normal to the line connecting the pair are taken. Thus we measure an average of only weakly distorted core distributions.

Figure 22 compares the $\omega(r)$ profiles for four values of F at $Re \simeq 5 \times 10^3$, at

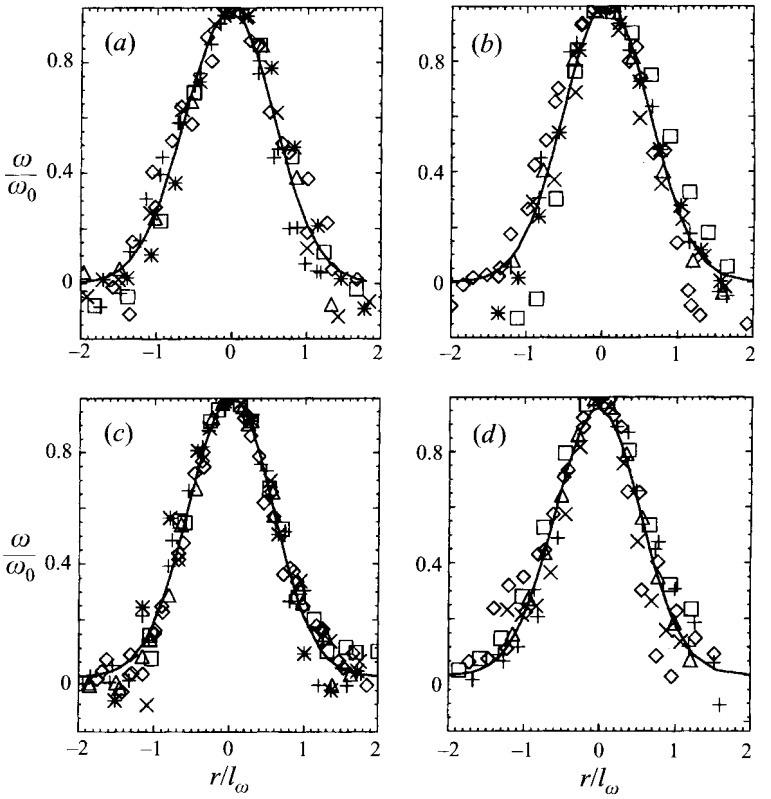

FIGURE 22. Radial distribution of the vertical vorticity (omitting subscript z) for R5: (*a*) R5.1, (*b*) R5.2, (*c*) R5.4, (*d*) R5.8, with F increasing from 1.2 to 7.9 from (*a*) to (*d*), all at time $Nt \approx 140$. 14, 12, 12 and 20 individual profiles are superimposed on each plot, but the symbols are not unique. The spacing of the square symbols in (*b*) indicates a typical spatial resolution. The solid curves are least-squares Gaussian fits to the ensemble-averaged profiles.

$Nt \simeq 140$. The residuals in the Gaussian fits do not vary systematically with F, and this functional form seems to approximate the data quite well. It is not uncommon to see negative tails in the data, that are probably attributable to transects running through the edge of an opposite-signed neighbour.

Somewhat more surprisingly, figure 23 shows that variations in Re do not have a measurable effect on the profile shape, which again is usually well approximated by a Gaussian. Recall that the lowest-Re cases (F10.1, F10.3, top rows, figure 8) have a much more fragmented, less smooth $\omega_z(x, y)$ distribution, which is not reflected in the cross-sections of figure 23.

Several explanations can be advanced: (i) a statistical average of a large number of arbitrary-shaped peaks could simply look like a Gaussian. However, there are no large deviations in the individual profiles, and the scatter of data around the solid line in F10.2, figure 23, is not greater than either the F10.7, F10.10 cases at higher Re, or the R5 series in figure 22. (ii) It could be a problem associated with the lower effective resolution (grid scale compared to body diameter) at lower Re. Cumulative smoothing effects could be such that the apparent Gaussian is just the average smoothing function convolved with initially non-smooth data. This possibility is hard to rule out entirely, despite the precautionary measures discussed in §2.3.6. In the worst case, there are only seven points across an entire individual profile, and

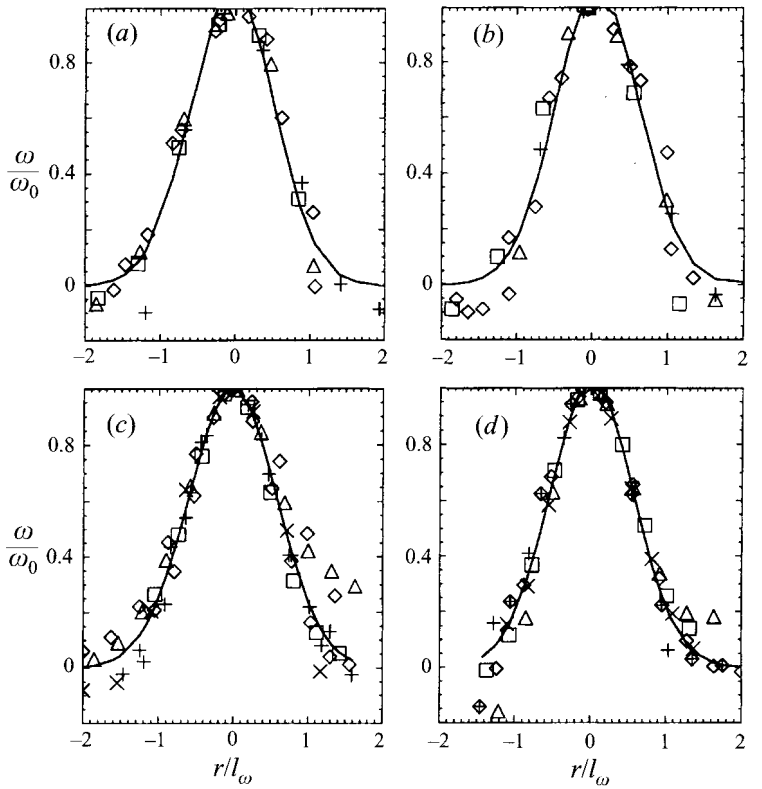

FIGURE 23. ω/ω_0 *vs.* r/l_σ for $Re = \{1685, 3300, 6715, 9880\}$ and $F = 10$ and $Nt = 140$ (from series F10: (*a*) F10.2, (*b*) F10.3, (*c*) F10.7, (*d*) F10.10). Further details as in figure 22.

sharp, subgrid-scale vorticity gradients might have been artificially smoothed out. On the other hand, data points *do* exist in the individual profiles in figure 23(*a,b*) that deviate from the mean, and from a perfectly smooth curve. It is also perfectly possible to measure $\omega(r)$ profiles over selected structures at the same scale that have much less regular shapes, and that have steeper gradients of $\partial\omega/\partial r$. Because the shapes of these strained vortices were clearly affected by interactions with other vortices, they were not included in figure 23. It is therefore demonstrably *not* the case that steeper, or less regular distributions of a similar scale cannot be measured. It *is* the case that those that have been selected are those that are apparently undistorted structures in the first place. Thus a reflection of the irregular $\omega_z(x, y)$ fields at low Re lies in the smaller *number* of profiles (compare F10.2, F10.3 in figure 23, with the others in that figure, and also with any of figure 22) that were subjectively judged to have met this criterion. Nevertheless, when one of these structures can be isolated, the vorticity distribution is not unlike that of higher-Re cases. Finally, therefore, we are left with the more prosaic explanation, (iii), that the $\omega(r)$ profiles really do look like this, perhaps due to similar fluid mechanics. In considering viscous vortices at these time scales, diffusion of vorticity could account for such similarity. When the vortex core structure differs substantially, as it does more frequently at low Re, then it does so because of increased frequency of vortex–vortex interactions.

Before further pursuing this point, we note without further graphical demonstration that the Gaussian form also fits the data well at all Nt, once the identifiable structure has formed, and provided it is not being stretched by strong neighbour interactions.

Since $\omega(r)$ can in general be written as

$$\omega(r) = \omega_0 e^{-(r^2/2l_\sigma^2)},$$

the time evolution of ω_0 and l_σ of individual wake vortices can be investigated, as can the circulation, Γ_σ, which can be integrated out to the radial distance, r_σ, where $r = l_\sigma$:

$$\Gamma_\sigma = 2\pi \int_0^{r_\sigma} \omega(r) \mathrm{d}r.$$

3.6.2. *The life history of a vortex*

An automated tracking algorithm was devised so that selected single vortices were tracked in reverse time, beginning at a frame of data with a small number of readily identifiable structures. An initial vortex, once labelled, can very easily be tracked automatically owing to the closely spaced timesteps (only every other timestep was ultimately used), and the well-organized nature of the flow field. At each timestep, an elliptical Gaussian fit was made to the vortex, where the location, amplitude, major and minor axes, and orientation are solved for in a six-parameter least-squares fit. Γ_σ is computed within this ellipse, but for simplicity l_σ is taken as the mean of the two length scales. When (in reverse time) a merger is observed, the partner is also picked up, labelled and tracked in the same fashion. Not many vortices can be followed for long times in this way (after all, few remain in the final frames), and so the following descriptions and observations necesarily lack statistical weight; nevertheless certain points can be made.

The time evolution of two vortices, one positive (+) and one negative ($\diamond$), from the same experiment (R5.8), can be seen in figure 24: l_σ, $|\omega_0|$ and $|\Gamma_\sigma|$ are plotted in dimensional units *vs.* time in buoyancy periods, Nt. The $\omega_z(x, y, Nt)$ fields for each data point are shown in figure 25, where the individual vortices are labelled with the same symbols as in figure 24. The tracking begins in the bottom right corner and proceeds from right to left, bottom to top in figure 25.

At long times, the increase in l_σ, and decay of $|\omega_0|$ and $|\Gamma_\sigma|$ with Nt are quite similar in the two vortices. During this period, which occupies most of the total time, the vortices apparently interact only weakly with like-signed neighbours, and process slowly, as a couple, in the direction of the mean wake flow, towards the left edge of the observation area. Despite the lack of obvious signs of vortex–vortex interactions in the plane, it is not necessarily equivalent to their being isolated. As already noted, this wake, and others at sufficiently high Re, is remarkable in its high degree of organization at long times, and this particular couple (if indeed it should be so termed) has not strayed far from the wake centreline, up to $Nt \simeq 1000$ ($x/D \simeq 4000$) in the final frame.

Early on, at $Nt = 77$ (timestep #5), a merger occurs between the positive vortex (+), and a neighbour, shown in figures 24 and 25 as a $\triangle$ symbol. At the moment of this merger, given by the solid white blobs in figure 25, both l_σ and $|\Gamma_\sigma|$ rise sharply for (+). This is followed by a short plateau in ω_0 for (+), as vorticity accumulates into a more compact structure. Consequently, l_σ drops quite rapidly. About $70Nt$ (4 timesteps) after the merger event, values of l_σ, $|\omega_0|$ and $|\Gamma_\sigma|$ appear to have relaxed back to values that might be extrapolated from pre-merger conditions. The rapid relaxation corresponds to momentarily very high decay rates of circulation in the plane, and either the merging process is extremely dissipative, or there is an out-of-isopycnal flux of circulation. The observed vertical flux could correspond to a readjustment in z of the vortex structure(s) with respect to the measurement

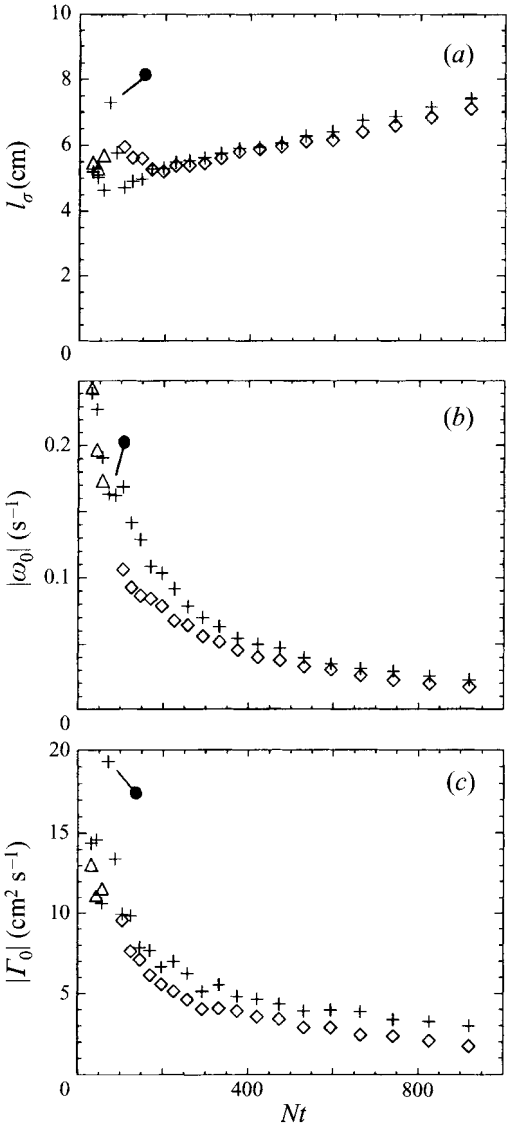

FIGURE 24. The evolution of vortex radius, l_σ (*a*), maximum amplitude, $|\omega_0|$ (*b*), and circulation, $|\Gamma_\sigma|$ (c), with Nt for two vortices in one experiment, $\{Re, F\} = \{5300, 7.8\}$ (R5.8). Early on, a third vortex, shown with △ symbol, appears briefly before merging with its (+) neighbour, at the point marked with the solid circle.

plane. Alternatively, the merger could be accompanied by vertical thickening of the wake, or give rise to a tilting of the vorticity vector into horizontally shearing structures. Fifteen merger events have been tracked in this way, and the interactions are sometimes conservative, in the sense that initial merged circulations are roughly equal to the sum of the component values before the merger, or non-conservative, with up to 80% of the circulation in the plane being removed during the merger. Statistically, one might expect that any mechanism involving layer thickening would depend in a predictable way upon the Froude number, but not enough measurements have been made to test this, and in any event, we have already noted how the *local*

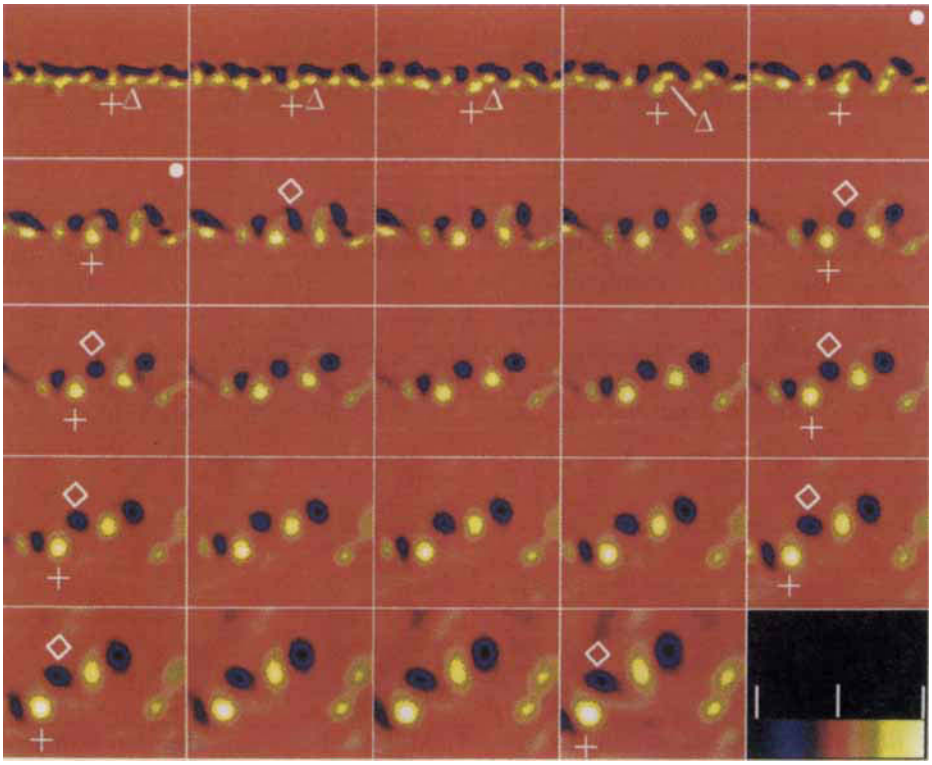

FIGURE 25. $\omega_z(x, y, t)$ for the same experiment as figure 24. The equivalent time and downstream ranges are: $Nt \in [21, 920]$, $x/D \in [82, 3620]$. There is a one-to-one correspondence between frames and symbols in the two figures, so each fluctuation in the curves of figure 24 can be matched to a particular event in a particular vortex here. The merger between (+) and (△) vortices occurs at the timesteps marked by the solid white blobs. Symbols are otherwise placed only at the beginning and end of each line to assist in visual tracking. The colour bar was designed to identify three primary regions: blues for negative vortices, reds for low absolute values, and yellows for positive vortices. The colour bar is rescaled at each timestep, and balanced symmetrically about zero, which is shown by the middle vertical bar. Tracking begins at bottom right and proceeds from right to left, bottom to top.

Froude number is always small (cf. figure 21). Moreover, there is no reason to suppose that either one of these mechanisms occurs to the exclusion of the other.

In each of the $\{Re, F\}$ pairs of figure 6, the time histories of the strongest surviving vortices at late times can be compared. The difference between vortices in figure 24 can be borne in mind as an indication of the likely variance within each $\{Re, F\}$ example.

3.6.3. *Dependence of vortex scaling on* $\{Re, F\}$

If motion in the vertical dimension is supressed by stratification, then the flow might behave locally as if it were two-dimensonal. Furthermore, one might reasonably ask whether the late-wake data collapse because all motion is basically governed by *viscous diffusion of vorticity*. Without going into great detail, a simple viscous model flow can be used for a heuristic comparison. The solution for the viscous decay of an initially isolated, two-dimensional vortex of strength Γ_0 was given by

Lamb (1932, §334a) as

$$\omega = \frac{\Gamma_0}{4\pi\nu t} e^{-r^2/4\nu t}, \tag{3.13}$$

for which the circulation at radius r is

$$\Gamma = \Gamma_0 \left(1 - e^{-r^2/4\nu t}\right). \tag{3.14}$$

The vortex size $r \sim t^{1/2}$, so a non-dimensional scale would grow $\sim t^{1/2}$. The vorticity, ω, decays $\sim t^{-1}$ and the circulation, Γ, would remain constant. These scalings provide a simple point of comparison for the measured l_σ, ω_0 and Γ_σ. Alternatively, one might use the turbulence velocity and length scale arguments that result in relations of the type in equations(3.4)–(3.6) to generate predictions and scalings that include stratification parameters. Thus, if measures of individual vortices behave as the flow field does in general, then length, vorticity and circulation should scale as

$$\left(\frac{l_\sigma}{D}\right) F^{-1/3} \sim (Nt)^{1/3}, \tag{3.15}$$

$$\left(\frac{|\omega_0|}{U/D}\right) F \sim (Nt)^{-1}, \tag{3.16}$$

and

$$\left(\frac{|\Gamma_\sigma|}{UD}\right) F^{1/3} \sim (Nt)^{-1/3}. \tag{3.17}$$

Note that the predicted exponents for l_σ and Γ_σ differ from the two-dimensional viscous diffusion model, but ω_0 is the same.

Figure 26 shows first that equations(3.15)–(3.17) are quite successful in collapsing the data over a range of F, and second that there are periods at moderate to late times where the exponent seems not unreasonable. $(l_\sigma/D)(Nt)$ (figure 26*a*) seems to contain two different regimes. Up to $Nt \approx 300$, there is a very gradual growth in l_σ/D, whose absolute values still show some remaining F-dependence that is not accounted for by the predicted $F^{-1/3}$ law. Interestingly enough, the data collapse quite well for a $F^{-1/2}$ scaling that might have been predicted had an $Nt^{1/2}$ behaviour been postulated. We include the customary caution here about interpretation of peculiar trends at early times that may reflect insufficient and unequally distributed effective sampling errors, but the result persists to quite late times ($Nt \approx 300$), far beyond the very early timesteps when uncompensated resolution errors could be at fault.

In the second regime, for $Nt > 300$, growth occurs at rates that are fairly consistent with the anticipated 1/3 law. The $t^{1/2}$ behaviour for purely two-dimensional viscous diffusion appears to significantly overpredict the observed growth rates. Of course, diffusion of vorticity occurs also in the vertical, and CH93*a* showed that the vertical diffusion occurs more rapidly than on viscous time scales, possibly due to an Ekman pumping type of mechanism. These, and other three-dimensional effects need to be accounted for in a suitable three-dimensional model.

The decay in peak vorticity magnitude (figure 26*b*) shows a good collapse and agreement with a t^{-1} scaling that would be expected both from viscous diffusion alone, and also from the foregoing, wake-averaged results. The Γ_σ decay rates are not so clean, but do not show significant disagreement with a $t^{-1/3}$ law. They are not zero.

Generally, the vortex time histories rescale just as the wake-averaged turbulence and mean flow quantities do, although the length scales show some persistent differences

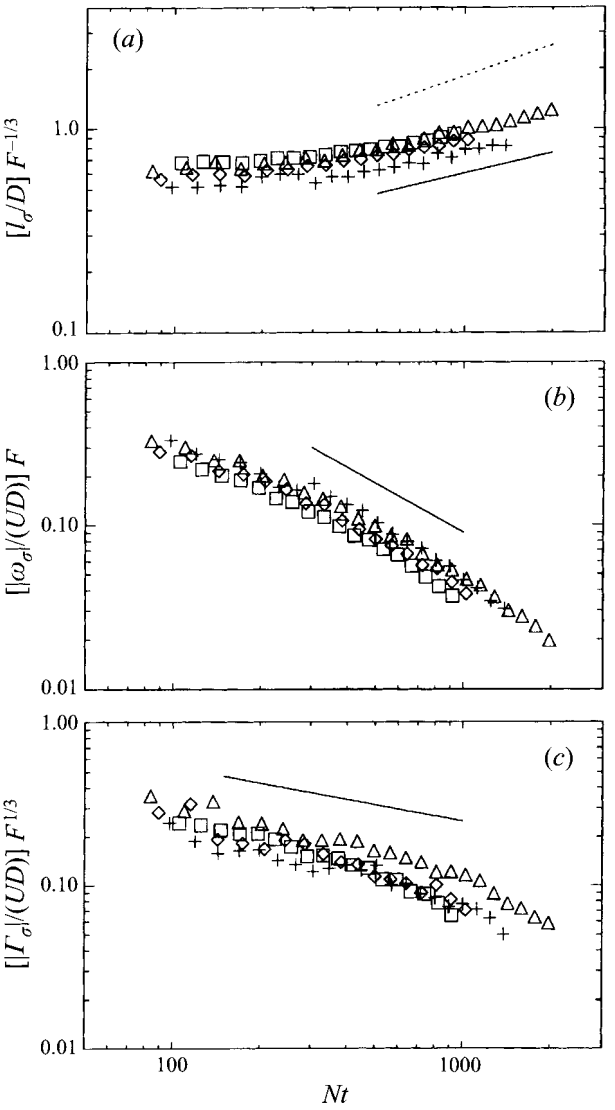

FIGURE 26. Normalized vortex radius, l_σ/D (*a*), peak vorticity, $|\omega_0|/(U/D)$ (*b*), and circulation magnitude, $|\Gamma_\sigma|/(UD)$ (*c*), rescaled by F as described in the text, for R5. $F = \{1.2, 2.0, 4.0, 7.9\}$ for symbols $\{+, \diamond, \triangle, \square\}$. The solid lines are from equations (3.15)–(3.17) respectively, drawn over the range of Nt where they might adequately describe the data. The dotted line in (*a*) is for an $Nt^{1/2}$ power law, with arbitrary offset.

at early times. A number of alternative scalings and normalizations were investigated, but all were measurably worse in collapsing the data. Recall that these are *still* basically modified scaling arguments derived for three-dimensional unstratified fluid turbulence. They provide no physical explanation as to why such such behaviour should be observed here; apparently, an explanation invoking the omnipresence of viscosity is insufficient, as the slopes of figure 26 do not scale this way.

Following the failure of low-Re data to collapse in the wake-averaged measurements, one might expect a similar result for individual vortex length scales, unless the apparent insensitivity of the shape to Re in figure 23 foreshadows similar behaviour

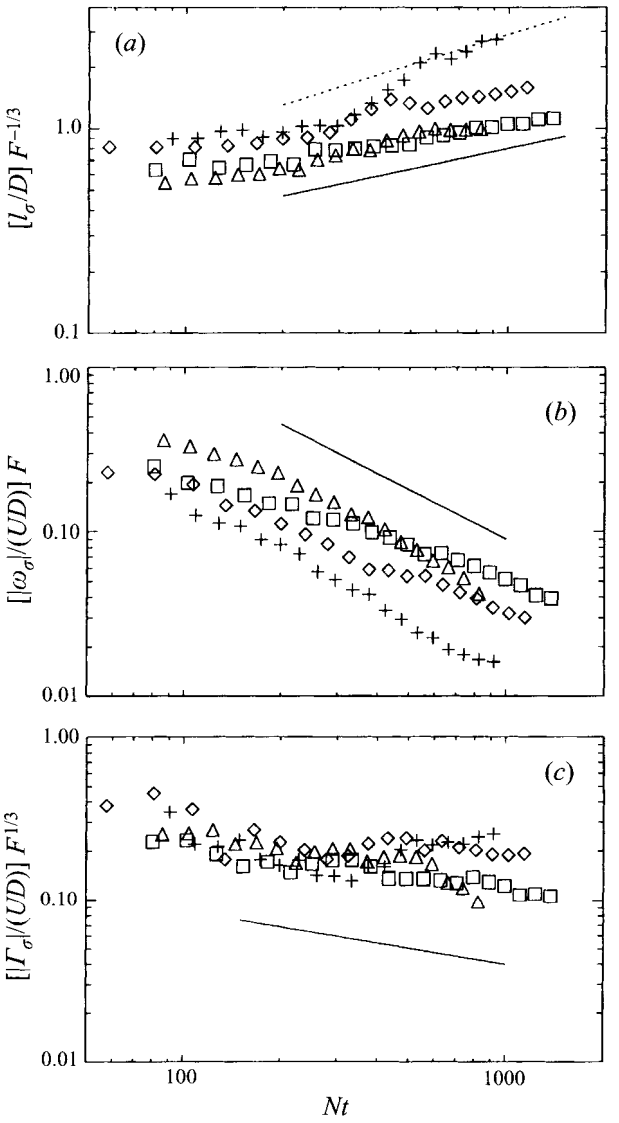

FIGURE 27. Normalized l_σ/D (*a*), $|\omega_0|/(U/D)$ (*b*), and $|\Gamma_\sigma|/(UD)$ (*c*) for F10, where $Re = \{1685, 3300, 6715, 9880\}$ for symbols $\{+, \diamond, \triangle, \square\}$. Further details as in figure 26.

in the scaling of the shape with time. Figure 27 is as figure 26, but for the F10 series. In all three graphs, the lower-*Re* curves, (+, ◇: $Re < 4 \times 10^3$) can be separated from the higher-*Re* ones (△, □: $Re > 6 \times 10^3$). The scales on the ordinates are the same as figure 26 and the higher-*Re* curves are consistent with those data at $Re \simeq 5 \times 10^3$. The mean radius shows considerable fluctuations at lower *Re*, and each of these these can be traced back to continuing interactions between wake vortices as the less-orderly wake geometry brings them into mutual contact. In the face of such variations it is difficult to determine whether or not the low-*Re* curves indeed show a more viscous-type scaling behaviour in l_σ (a possible interpretation of figure 26*a*), but their $\Gamma_\sigma(Nt)$ curves are almost flat, as would be the case in a purely two-dimensional viscous decay.

Consistent with previous results in this paper, the low-Re data do not show the same scaling behaviour as the higher-Re data. The transition value appears to be some where in the range 4–5 $\times 10^3$.

4. Discussion

4.1. *Scaling of stratified turbulent wakes*

Existing data on three-dimensional turbulent wakes behind bluff bodies show scaling behaviour that one might perhaps expect to be followed at early times in stratified wakes, at sufficiently high values of Re and F. Eventually, however, one might equally expect to see significant departures, due to the increasingly effective suppression of vertical scales of motion in the decaying wake. The unmodified three-dimensional arguments are surprisingly good estimators for the exponents in power law behaviour of mean profile velocity and length scales, and a simple recouching of these physical assumptions into stratification parameters is successful in collapsing both mean profile and wake-averaged turbulence measurements. The initial decay rates appear to hold for very long times, up to $Nt \approx 1000$ ($400 \leqslant x/D \leqslant 4000$). After this Nt, the decay rates of the wake energy and enstrophy increase, but the surprising aspect is that the three-dimensional scaling works for so long. In the regime, $100 < Nt < 1000$ the vertical velocity, w, is very much smaller than $\{u,v\}$, and the flow is neither three-dimensional, nor turbulent (local mean $\langle Re \rangle \leqslant 10^3$). Of course, a demonstrated agreement with some postulated scaling argument does not in itself constitute a proof of physical mechanism. In three-dimensional turbulent axisymmetric wakes, application of the self-preservation hypothesis to the reduced momentum equations (Tennekes & Lumley 1972) leads to $l \sim x^{1/3}$ and $U \sim x^{-2/3}$. For plane wakes the relations are $l \sim x^{1/2}$ and $U \sim x^{-1/2}$, respectively. In these, and all other measures reported here, the stratified wakes are better approximated by three-dimensional scaling relations than by two-dimensional or plane wakes. It is possible that some structure in the vertical direction allows dynamical interactions that give averaged scaling laws that are similar to the three-dimensional results.

4.2. $\{Re, F\}$-*dependence*

One common thread linking these arguments is the assumption of a fully developed turbulence, where only local scales of length and velocity determine the flow. It is unsurprising therefore, to find that there is a certain minimum Re before such scaling regimes obtain. Measures proportional to the wake width, kinetic energy, enstrophy, vortex size, peak amplitude and circulation all fail to collapse when $Re < 5 \times 10^3$. The maximum Re for which collapse has been demonstrated (i.e. the highest Re attained in the experiments) is 2×10^4. Apparently, the initial Re determines conditions that are felt even into the far-wake dynamics. The local, far-wake Re-variation with initial Re, shown in figure 21, demonstrates that some such effect exists. A reasonable interpretation is that the late-wake Re must be large enough to ensure essentially inviscid dynamics there.

The issue of Re-dependence is of some relevance since one objective is to establish results that can be extrapolated to practical ocean applications. There is no Re-dependence in the postulated dynamics leading to the scaling arguments of equations (3.4)–(3.6), and explanations cannot involve F-related physical processes, since the Re-dependence can be measured at constant F. The solution must be related to the initial range of scales available, or the way in which energy is distributed among them, and it is possible that some kind of self-similar cascading range must be established

so that the ultimately stable vortex patches can emerge from initial conditions that possess characteristics of an Re-independent turbulence. This requirement might also be regarded in terms of the disruption of small-scale anisotropies or breaking of local vortex loops and connections that serve in the long run to destabilize the wake structure. Certainly, the most noticeable trait of the low-Re wakes is their relatively disorderd state in the (x, y)-plane, and continued interactions amongst their component vortices lead to high-amplitude fluctuations about the mean profile.

An interpretation can also be made that considers the transition from convective to absolute instability of the helical mode in the wake. Monkewitz (1988) showed that the first helical mode is absolutely unstable when $Re > 3.3 \times 10^3$ for (unstratified) bluff body wakes, and suggested that large-scale helical vortex shedding in the Re range $[6 \times 10^3,\ 3 \times 10^5]$ noted by Achenbach (1974), could be driven by self-excited oscillation in the near wake. CH93*b* also noted an apparent strengthening of the spiral instability mode for $Re \geqslant 4 \times 10^3$ and $F \geqslant 4.5$ in stratified wakes.

The somewhat limited evidence here suggests that the higher-Re data may be representative of a larger range of Re, where at least the wake-averaged scaling behaviour does not depend on Re. Although we assume the existence of such an Re-independent turbulence at sufficiently high Re, the issue remains controversial in some flows (e.g. Miller & Dimotakis 1991), and further careful measurements are required.

The requirement for a minimum F seems intuititively reasonable and Spedding *et al.* (1996) gave a simple scaling argument for an expected minimum value of $F \geqslant 3$ for active turbulence on all scales in a stratified fluid. However, when Re-independent collapse in the turbulence data is achieved (figures 10, 12, 13, 14), it is over the entire range of $F \in]1.2, 30[$, with no evidence that $F = 4$, or thereabouts, represents a critical or special value in this regard. Furthermore, although the dimensionless wake spacing, St, is a function of F, and takes an initial value commensurate with helical shedding modes only at $F \geqslant 4$ (figure 17), it is not a strong function of Re, at any given F. Therefore, if it is true that the initial St reflects the strength of the near-wake helical mode forcing, then this forcing is not strongly dependent on Re over the range $Re \in]1216, 9880[$ (figure 17*b*,*c*). By the same token, if it is true that the strong global mode appears only at $F \geqslant 4$, then it cannot provide a sufficient explanation for the Re-dependence in turbulence quantities, because the Re-dependent variations were measured at Froude numbers both higher and lower than this putative critical value.

The general absence of Froude number dependence in the turbulence and mean wake profile data collapse (as noted above, in figures 10, 12, 13, 14), in local measures of $\langle F \rangle, \langle Re \rangle$ (figure 21), and in the geometry and evolution of individual vortex cross-sections (figures 22, 26) is rather surprising. At some sufficiently large value of F, the wake defect velocity ought to converge on the unstratified result, but such a trend was not observed for $F \leqslant 30$. At lower Froude numbers (typically $0.1 \leqslant F \leqslant 2$), the strong influence of F on the near-wake shedding and wake development has been well-documented (e.g. Sysoeva & Chashechkin 1991; Chomaz *et al.* 1992; Lin *et al* 1992; CH93*b*), but the late-wake measurements do not appear to reflect these changes. Two points need to be made: first, the power law measurements have only been made for the late wake, and at one measurement plane. It would be incorrect to conclude either that the power law behaviour is constant through early- and late-wake evolution, or that the same dynamics govern motions in the vertical. On the contrary, it is clear that in order for the mean centreline velocity to be both higher in magnitude *and* decaying at a similar rate to three-dimensional wakes, the earlier wake decay must have been much weaker. Furthermore, even

though the decay rates are the same as for three-dimensional wakes, the resemblence is superficial. We are far from three-dimensional turbulent motion in the late wake, where $w \ll \{u, v\}$. The dynamics of motions effectively confined to a plane might be thought of as essentially two-dimensional, and comparisons with two-dimensional turbulent motions are inviting. But the dynamics are not two-dimensional either (the decay rates of L_σ/D and U_0/U with x/D in table 2 are more than two standard deviations away from the $1/2$ and $-1/2$ values expected in a turbulent plane wake), and the dynamics governing the vertical wake growth, as considered carefully in CH93*a*, can be expected to modify the horizontal growth rates. It looks as though these particular results will not be fully understood until simultaneous, quantitative measurements of the vertical structure and evolution have been made, and for earlier times that precede the quasi-two-dimensional motions.

4.3. *Detection criteria*

The detectability and persistence of a given wake flow depends on the mean defect magnitude, the wake width and geometry (i.e. distribution of $\omega_z(x, y)$). It is interesting to note, therefore, that while the increase in dimensionless wake width with time scales as three-dimensional wakes do, the stratified wake is *narrower* than the homogenous wake, increasingly so as F decreases, i.e. as buoyancy forces become more significant. We have shown here, for the first time, that the mean centreline velocity is up to one order of magnitude higher than for the same unstratified wake flow, consistent with the one data point that can be inferred from the existing literature.

Both obervations can be attributed to the high degree of order in the wake, which is composed of arrays of vortex patches that do not move far from the centreline. It appears to be a naturally preferred arrangement, in that the ordered array emerges from an initially very disorganized, turbulent flow. Even at the highest F and Re (about 30 and 2×10^4, respectively), an ordered array of vortices results, and maintains the mean wake flow for much longer than would otherwise be the case. A preferred topology of wake vortices could also explain the reduced wake spreading rate.

An immediate practical consequence of the tightly packed, structured array, is that mean wake-averaged energy and enstrophy densities can be detected above experimental noise for very long times, equivalent to 12 days in a stratified ocean. The *pattern* of $\omega_z(x, y)$ is also observable for such periods. Because the wake vortices persist as coherent material patches, inhomogeneities of passive scalars, once trapped in a vortex core, could remain at concentrations significantly above ambient for extended periods. Such scalars could include trace chemicals from the body, or plankton in the environment.

4.4. *The geometry of the vorticity field*

4.4.1. *Reduced spatial intermittency*

Some of the statistical or wake-averaged quantities above can be related to the wake structure and geometry through the general concept of reduced spatial intermittency. Since the vertical velocity, w, is effectively zero, there is no temporal variation in the z-location of the wake. Consequently, if kinetic energy cannot propagate or fluctuate strongly in the vertical (this is almost true at late times when the internal wave motions are of low amplitude), owing to the confining effects of stratification, and since the lateral growth rate is *not* correspondingly increased, then the local wake energy density close to the centreline must be correspondingly increased. Alternatively, if one thinks of the stratified wake as a collapsed helical structure, then the concentration of wake motions onto the centreplane will increase the energy density there.

4.4.2. *Vortex cross-sections*

Measurements of $\omega_z(r)$ in the centreplane indicate that individual vortex profiles have close to Gaussian shape over most of the range of F, Re and Nt discussed here. The result is applicable only to those vortex structures that have formed as separate features, and deliberately excludes from consideration all those that are being deformed due to strong interactions with neighbours. The statistics of the low-Re, wake-averaged quantities differ from their high-Re counterparts not because the vortices are fundamentally different in cross-section, but because they undergo more frequent, strong, interactions with nearby vortices. A Gaussian vortex core distribution would be a good model approximation for any of the flow fields. The cross-sections are circular in the absence of any external strain field.

The apparently universal structure may suggest some general physical explanation, and diffusion of vorticity could account for a similar smoothing of all steep vorticity gradients over the long time scales of the present experiments. However, the growth/decay rates of vortex radius, maximum vorticity and circulation do not agree well with the most simple two-dimensional viscous diffusion model, but instead reflect the same scaling behaviour as the wake as a whole. This includes the lack of collapse of the low-Re data. The need for a more realistic, three-dimensional model seems clear.

4.4.3. *Vortex interactions*

In the measurement plane, the most noticeable vortex–vortex interactions were between like-signed neighbours. Usually two were involved; occasionally, at early times, three. The Strouhal number in the late wake decreases with time as successive mergers decrease the number of vortices per unit length in X. St is independent of Re (within experimental uncertainty) over the range of Re studied, and was found to decrease with $F^{-1/3}$, consistent with the scaling behaviour of the other measured length scales: the wake width, L_W, and the vortex radius, l_σ. Mutual deformation and loss of vertical axisymmetry were observed during merging events, but afterwards the remaining single vortex would quickly relax back close to a circular geometry, without any further pairing interactions.

Vortex couples (Couder & Basdevant 1986), dipoles (Voropayev & Afanasyev 1992; Flór & van Heijst 1994; Flór, van Heijst & Delfos 1995) and quadrupoles (Voropayev, Afanasyev & van Heijst 1995) are frequently discussed as canonical objects in terms of which more complex flows may be described, but the wake vortices here show little tendency to preferentially form such groupings. In particular, *isolated* couples which can progagate far from their original point of origin do not emerge. When couples can be identified in these experiments (e.g. for convenience in figure 25), they do not appear to be dynamically distinct entities. Instead, there appears to be a degree of structure and coherence to the whole wake.

4.4.4. *Vertical structure*

Vertical layers in stratified wakes

It is well established that strongly turbulent patches in a stable stratification develop into distinct layers that are limited in vertical extent by the background stable density gradient (e.g. Browand *et al.* 1987). The inhibition of vertical scales of motion as a function of internal Froude number in turbulent wakes of towed and self-propelled slender bodies was reported by Lin & Pao (1979), who also noted the development of layered motions in stratified wakes. CH93*a* discuss the different wake regimes that occur with different F, designating $F = 4.5$ (as defined here) as a nominal critical

value above which multiple layer formation can be expected. Since our investigation is thus far confined to measurements along an isopycnal, deductions concerning vertical structure are limited, but a self-consistent and testable model can be proposed.

How many layers?

There is no hard evidence for the number of layers in stratified wakes, and how it varies with F. A first estimate can be made through the Osmidov length scale argument, where the maximum vertical scale, l_0 is

$$l_0 = \left(\frac{u^3}{lN^3}\right)^{1/2} \approx \left(\frac{\epsilon}{N^3}\right)^{1/2}, \tag{4.1}$$

where l is a turbulent integral length scale and ϵ is the kinetic energy dissipation rate. If we assume that initial turbulent length scales are proportional to the sphere diameter, D, then the number of layers per unit diameter can be written

$$\frac{D}{l_0} \sim F^{-3/2}. \tag{4.2}$$

The number of layers increases with decreasing F. CH93*a* observe a minimum F required for multiple layer formation, arguing that only at sufficiently high F can the spiral instability mode be fully active over an extended vertical range, and the individual collapse of subranges provides the breakup into distinct layers. The two arguments together imply the existence of a value of $F \simeq 4$ that gives a maximum number of layers. Much remains to be learned concerning their formation and dynamical significance.

Three-dimensional geometry

Indirect evidence suggests a plausible three-dimensional structure that can be tested in future investigations. The vertical vorticity has been comprehensively described, but what then becomes of the vortex lines? When exterior boundaries are far away, vortex lines must reconnect to form closed loops. Related experiments indicate how this may occur.

Fincham, Maxworthy & Spedding (1996) proposed a model for a preferred arrangement of densely packed, discus-shaped vortex patches in decaying, stratified grid turbulence, where vortex lines are free to meander through nearby patches in both horizontal and vertical directions. The model was supported by data in vertical slices that revealed the predicted horizontal vortex sheets between layers. The vertical correlation of vortex structures at different heights behind a single vertical bar was also investigated (see Fincham 1994) by injecting green and red dye at $z = H/3$ and $2H/3$ respectively (where H is the total fluid depth) at the separation point. Although initially correlated, the wake vortices quickly took up locations that were 180° out of phase with respect to their like-signed neighbours in z, and remained there.

Consequently, the following arrangement of vortex lines in a stratified bluff body wake can be proposed. In a single layer, vortex lines can connect in a chain of vortex loops (figure 28*a*), whose vertical extent is controlled by the stratification, as argued above. It is a stratified equivalent of a Kármán vortex street. When there are multiple layers, successive lamina in z are not completely decoupled, but have preferred offset locations, so that wake vortices reside in arrays that are staggered in both horizontal and vertical directions. Figure 28(*b*) shows a schematic for the topology for two layers. The model is fully consistent with the observed distribution of ω_z in the centreplane (certain alternative configurations can be ruled out from the $\omega_z(r)$ profiles of figures 22

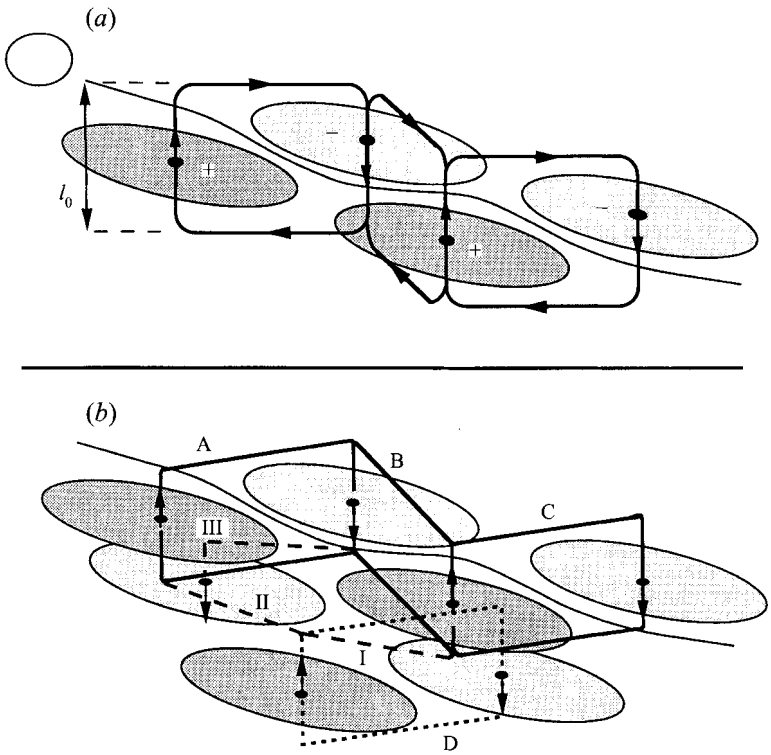

FIGURE 28. (*a*) Vortex lines loop between opposite-signed partners in a stratified version of the classical Kármán wake, where the Osmidov scale, l_0, controls the vertical thickness. (*b*) The vortex loops of part (*a*) are labelled A, B and C. A second layer has been added, with one loop (D) shown in short dashed lines. Possible connections are no longer restricted to within each layer, and D can connect up to C and A through lines I and II, and similarly, A can pass *via* III to the lower layer.

and 23). Judging by the persistent, compact nature of $\omega_z(x, y)$ reported here, the wake structure is very robust, and it is possible that stratification enforces a proximal bending of vortex lines that promotes local interconnections. Once formed, the chain does not break easily.

The single-layer model of figure 28(*a*) is topologically quite similar to the one proposed by Pao & Kao (1977), except that no special assumption is made here concerning the origin of the vortex structures from the sphere surface. On the contrary, a minimum *Re* appears necessary for the formation of such an ordered array, so fully turbulent flow must be initially present in the near wake. Preceding arguments suggest also a minimum F requirement, but measurements reported here do not clearly show it.

Once formed, the multilayer wake is neither a series of decorrelated, largely independent horizontal layers, nor a stack of loosely correlated patches that are coupled and uniform in the vertical, but rather a quite closely coupled series of interconnected vortex patches that reside in particular offset locations with respect to their neighbours above and below. An analogy can be made with a necklace, where vortex lines weave in and out through neighbouring wake elements, or vortex patches, within and between layers. The necklace wake is a naturally-preferred arrangement of high-aspect-ratio vortices in a stable stratification, one that emerges from turbulent and disordered initial conditions.

Dynamical significance

Fincham *et al.* (1996) demonstrated that vertical layering in stratified grid turbulence is responsible for a large fraction of the kinetic energy dissipation. The surfaces of constant dissipation are highly anisotropic, up to 90% of the dissipation originating at thin horizontal vortex sheets. Recalling the collapse of wake turbulence quantities, the exceptional case was in the kinetic energy dissipation rate, ϵ_z, as measured by horizontal gradients of horizontal velocity. ϵ_z does not show the same collapse as the other data, or the same failure to collapse at low *Re*. The fact that ϵ_z does not scale as the actual kinetic energy does argues for the comparative unimportance of this term in the total dissipation budget, which may again be dominated by inter-layer shearing. It is unclear as to how the anisotropy of the terms contributing to the total dissipation, ϵ, will affect arguments that assume $\epsilon \sim u^3/l$ (for example, those leading to equations (3.6),(4.1)).

4.5. *Open questions*

It is quite clear that a full understanding of the stratified wake problem requires a three-dimensional model and corresponding three-dimensional data. The tentative model sketched out above can be explicitly tested with vertical profiles that will show the magnitude of the horizontal vorticity components, and how (and whether) the development of layers occurs.

It is possible that the special geometry and topology of vortex lines in the towed sphere wake does not generalize to other configurations, or to more general problems of the evolution of isolated turbulent patches (although the similarity with the phenomena described by Fincham *et al.* (1996) argues against this pessimistic view). It will therefore be instructive on both fundamental and applied practical levels to perform similar measurements on different body geometries and generating conditions: slender and/or self-propelled bodies come to mind.

With regard to practical application, and generalization of these results to oceanographic problems, it is especially important to attempt to model high-*Re* flows. This has been a point of contention in extending laboratory-based results and reconciling them with field measurements (e.g. Gargett, Osborn & Nasmyth 1984). The requirements of a reasonable range of scales, and/or global resonance of the helical shedding mode have been proposed as possible explanations for the departure from similarity of the low-*Re* wakes. An $Re_{min} \approx 5 \times 10^3$ appears to be a necessary condition, but similar scaling of most measures was obtained over all $F \in [1, 30]$, the exception being the late-wake streamwise spacing. Presumably, at some sufficiently high values of F, the wake will be indistinguishable from an unstratified wake. This should be tested. Likewise, extension to higher *Re* beyond the current maximum value of 2×10^4 would be highly reassuring.

The support provided by ONR Grant no. N00014-92-J-1062, administered by Dr L. P. Purtell, is most gratefully acknowledged.

Appendix. Retrieval of image data via internet

Images of $\omega_z(x, y, t)$ and $\Delta_z(x, y, t)$ can be viewed and/or downloaded on the World Wide Web, at URL:

`http://ae-www.usc.edu/rsg/gfd/wakes_index.html`

The images are in GIF or JPEG format, and have been compressed, with some

information loss. $\{Re, F\}$ pairs in the range $Re \in [10^3, 2 \times 10^4]$, $F \in [1, 30]$ can be selected from a forms table, and an INFO button for each $\{Re, F\}$ pair details the exact experimental conditions, including Nt for each frame in the time series.

REFERENCES

ACHENBACH, E. 1974 Vortex shedding from spheres. *J. Fluid Mech.* **62**, 209–221.

BEVILAQUA, P. M. & LYKOUDIS, P. S. 1978 Turbulence memory in self-preserving wakes. *J. Fluid Mech.* **89**, 589–606.

BONNETON, P., CHOMAZ, J. M., HOPFINGER, E. J. & PERRIER, M. 1996 The structure of the turbulent wake and the random wave field generated by a moving sphere in a stratified fluid. *Dyn. Atmos. Oceans* **23**, 299–308.

BROWAND, F. K., GUYOMAR, D. & YOON, S. C. 1987 The behaviour of a turbulent front in a stratified fluid: experiments with an oscillating grid. *J. Geophys. Res.* **92**, 5329–5341.

CHOMAZ, J. M., BONNETON, P., BUTET, A. & HOPFINGER, E. J. 1993*a* Vertical diffusion in the far wake of a sphere moving in a stratified fluid. *Phys. Fluids* A **5**, 2799–2806 (referred to herein as CH93*a*).

CHOMAZ, J. M., BONNETON, P., BUTET, A., PERRIER, M. & HOPFINGER, E. J. 1992 Froude number dependence of the flow separation line on a sphere towed in a stratified fluid. *Phys. Fluids* A **4**, 254–258.

CHOMAZ, J. M., BONNETON, P. & HOPFINGER, E. J. 1993*b* The structure of the near wake of a sphere moving horizontally in a stratified fluid. *J. Fluid Mech.* **254**, 1–21 (referred to herein as CH93*b*).

COUDER, Y. & BASDEVANT, C. 1986 Experimental and numerical study of vortex couples in two-dimensional flows. *J. Fluid Mech.* **173**, 225–251.

DALLARD, T. & SPEDDING, G. R. 1993 *2D* wavelet transforms: generalisation of the Hardy space and application to experimental studies. *Eur. J. Fluid Mech.* B **12**, 107–134.

FARGE, M. 1992 Wavelet transforms and their application to turbulence. *Ann. Rev. Fluid Mech.* **24**, 395–457.

FERNANDO, H. J. S., HEIJST, G. J. F. VAN & FONSEKA, S. V. 1994 The evolution of an isolated turbulent region in a stratified fluid. *J. Fluid Mech.* (submitted).

FINCHAM, A. M. 1994 The structure of decaying turbulence in a stably stratified fluid, using a novel DPIV technique. PhD thesis, Department of Aerospace Engineering, University of Southern California.

FINCHAM, A. M., MAXWORTHY, T. & SPEDDING, G. R. 1996 Energy dissipation and vortex structure in freely-decaying, stratified grid turbulence. *Dyn. Atmos. Oceans* (in press).

FINCHAM, A. M. & SPEDDING, G. R. 1996 Low-cost, high-resolution DPIV for turbulent flows. *Exps. Fluids* (submitted).

FLÓR, J. B., FERNANDO, H. J. S. & HEIJST, G. J. F. VAN 1994 The evolution of an isolated turbulent region in a two-layer fluid. *Phys. Fluids* **6**, 287–296.

FLÓR, J. B. & HEIJST, G. J. F. VAN 1994 Experimental study of dipolar vortex structures in a stratified fluid. *J. Fluid Mech.* **279**, 101–134.

FLÓR, J. B., HEIJST, G. J. F. VAN & DELFOS, R. 1995 Decay of dipolar vortex structures in a stratified fluid. *Phys. Fluids* **7**, 374–383.

GARGETT, A. E., OSBORN, T. R. & NASMYTH, P. W. 1984 Local isotropy and the decay of turbulence in a stratified fluid. *J. Fluid Mech.* **144**, 231–280.

GIBSON, C. H., CHEN, C. C. & LIN, S. C. 1968 Measurements of turbulent velocity and temperature fluctuations in the wake of a sphere. *AIAA J.* **6**, 642–649.

HOPFINGER, E. J. 1987 Turbulence in stratified fluids: a review. *J. Geophys. Res.* **92**, 5287–5303.

KIM, H. J. & DURBIN, P. A. 1988 Observations of the frequencies in a sphere wake and of drag increase by acoustic excitation. *Phys. Fluids* **31**, 3260–3265.

LAMB, H. 1932 *Hydrodynamics.* Dover.

LESIEUR, M. 1993 *Turbulence in Fluids.* Kluwer.

LIGHTHILL, M. J. 1978 *Waves in Fluids.* Cambridge University Press.

LIGHTHILL, M. J. 1996 Internal waves and related initial-value problems. *Dyn. Atmos. Oceans* (in press).

LILLY, D. K. 1983 Stratified turbulence and the mesoscale variability of the atmosphere. *J. Atmos. Sci.* **40**, 749–761.

LIN, J. T. & PAO, Y. H. 1979 Wakes in stratified fluids: a review. *Ann. Rev. Fluid Mech.* **11**, 317–338.

LIN, Q., LINDBERG, W. R., BOYER, D. L. & FERNANDO, H. J. S. 1992 Stratified flow past a sphere. *J. Fluid Mech.* **240**, 315–354.

MILLER, P. L. & DIMOTAKIS, P. E. 1991 Reynolds number dependence of scalar fluctuations in a high Schmidt number turbulent jet. *Phys. Fluids* A **3**, 1156–1163.

MONKEWITZ, P. A. 1988 A note on vortex shedding by axisymmetric bluff bodies. *J. Fluid Mech.* **192**, 561–575.

PAO, H. P. & KAO, T. W. 1977 Vortex structure in the wake of a sphere. *Phys. Fluids* **20**, 187–191.

PARK, Y.-G., WHITEHEAD, J. A. & GNADADESKIAN, A. 1994 Turbulent mixing in stratified fluids: layer formation and energetics. *J. Fluid Mech.* **279**, 279–311.

RILEY, J. J., METCALFE, R. W. & WEISSMAN, M. A. 1981 Direct numerical simulations of homogeneous turbulence in density stratified fluids. In *Nonlinear Properties of Internal Waves* (ed. B. J. West), pp. 79–112. AIP.

SPEDDING, G. R., BROWAND, F. K. & FINCHAM, A. M. 1996 The long-time evolution of the initially-turbulent wake of a sphere in a stable stratification. *Dyn. Atmos. Oceans* (in press).

SPEDDING, G. R. & RIGNOT, E. J. M. 1993 Performance analysis and application of grid interpolation techniques for fluid flows. *Exps. Fluids* **15**, 417–430.

STAQUET, C. & RILEY, J. J. 1989 A numerical study of a stably-stratified mixing layer. In *Turbulent Shear Flows* (ed. J. C. Andre, J. Cousteix, F. Durst *et al.*), vol. 6, pp. 381–397. Springer.

SYSOEVA, E. Y. & CHASHECHKIN, Y. D. 1991 Vortex systems in the stratified wake of a sphere. *Izv. Akad. Nauk SSSR, Mekh. Zhidk. Gaza* **4**, 82–90.

TENNEKES, H. & LUMLEY, J. L. 1972 *A First Course in Turbulence.* MIT Press.

UBEROI, M. S. & FREYMUTH, P. 1970 Turbulent energy balance and spectra of the axisymmetric wake. *Phys. Fluids* **13**, 2205–2210.

VOROPAYEV, S. I. & AFANASYEV, Y. D. 1992 Two-dimensional vortex-dipole interactions in a stratified fluid. *J. Fluid Mech.* **236**, 665–689.

VOROPAYEV, S. I., AFANASYEV, Y. D. & HEIJST, G. J. F. VAN 1995 Two-dimensional flows with zero net momentum: evolution of vortex quadrupoles and oscillating grid turbulence. *J. Fluid Mech.* **282**, 21–44.